Synchronization Phenomena in Spin Torque and Spin Hall Nano-Oscillators

Synchronization Phenomena in Spin Torque and Spin Hall Nano-Oscillators

Afshin Houshang

UNIVERSITY OF GOTHENBURG

Doctoral Dissertation in Physics

Department of Physics
University of Gothenburg
412 96 Gothenburg, Sweden

June 9, 2017

ISBN: 978-91-629-0215-5 (printed)
ISBN: 978-91-629-0216-2 (pdf)
URL: http://hdl.handle.net/2077/52045

Cover: Top: Schematic of the simulated spin wave propagation pattern for two vertically located nano-contact spin torque oscillators. The green arrow shows the spin wave propagation direction which is highly asymmetric due to the specific ferromagnetic resonance landscape, induced by the Oersted field. Bottom: The calculated ferromagnetic resonance landscape induced by the Oersted field for two vertically located NCSTOs.

Printed by Kompendiet, Gothenburg, 2017

Typeset using LuaLaTeX

"Somewhere, something incredible is waiting to be known!"

Carl Sagan

Abstract

Spin-torque oscillators (STOs) belong to a novel class of spintronic devices and exhibit a broad operating frequency and high modulation rates. STOs take advantage of several physical phenomena such as giant magnetoresistance (GMR), spin Hal effect (SHE), spin-transfer torque (STT), and tunneling magnetoresistance (TMR) to operate. In this work, it has been attempted to understand and study the excited magnetodynamical modes in three different classes of STOs i.e. nanocontact STOs (NCSTOs), spin Hall nano-oscillators (SHNOs), and hybrid magnetic tunnel junctions (MTJs). Synchronization has been considered as a primary vehicle to increase the output power and mode uniformity in NCSTOs and SHNOs. In the quest to achieve high signal quality for applications, a completely new class of devices, hybrid MTJs, has been studied. Therefore this work can be principally divided into three parts:

GMR-based NCSTOs: Synchronization has been shown to be mediated by propagating spin waves (SWs). The Oersted magnetic field produced by the current going through the NCs can alter the SW propagating pattern. In this work, the synchronization behavior of multiple NCs has been studied utilizing two different orientations of NCs.The Oersted field landscape is shown to promote or impede SW propagating depending on the device geometry. Synchronization of up to five NCs, a new record, is thus achieved. It is shown that the synchronization is no longer mutual in nature but driven by the NC from which the SWs are emitted.

SHNOs: The basic operation and characterization of SHNOs are demonstrated through electrical measurement and confirmed by micromagnetic simulations. Ultra small constrictions are fabricated and shown to possess ultra-low operating currents and an improved conversion efficiency. High efficiency mutual synchronization of nine SHNOs is demonstrated. Furthermore, by tailoring the connection region, the synchronization range can be extended to 4 μm. Furthermore, for the first time the synchronization state is directly probed utilizing micro-Brillouin light scattering.

Hybrid MTJs: While MTJs based oscillators utilizing a nanopilar geometry have been shown to deliver output powers much greater than GMR-based NCSTOs, they often suffer from higher linewidths. A hybrid device is fabricated to combine the high output power of nanopillar MTJs and low linewidths of NCSTOs. Realization of such devices is demonstrated and, for the first time, their magnetodynamical behavior is meticulously studied. Experimental results show evidence of both localized and propagating SW modes. Generating propagating SWs in these devices paves the way for synchronizing multiple hybrid MTJs sharing the same free layer, thus improving the oscillator performance.

Contents

List of Figures

List of Symbols and Abbreviations

List of Symbols

α	Gilbert damping constant
H, H_{ext}	external magnetic field
I_{dc}	bias current
H_{ext}	external magnetic field
H_{Oe}, H_I	Oersted magnetic field
H_{eff}	effective magnetic field
H_{dip}	magnetodipolar field
H_{ex}	exchange field
H_A, H_k	anisotropy field
H_{int}	internal magnetic field
θ_{ext}	external magnetic field angle
θ_{int}	out-of-plane angle of the magnetization
θ_c	critical angle
θ_{SH}	spin Hall angle
Ψ_{IP}	in-plane angle
M	magnetization
M_0, M_s	saturation magnetization
P	integrated power
p	spin polarization
R_P	resistance in the parallel state
R_{AP}	resistance in the antiparallel state
ρ	resistivity
D	spin density
σ^s	spin Hall conductivity
σ^s	charge conductivity
$\Delta f, \Delta H$	linewidth
ΔH_0	inhomogeneous broadening
f_{NC}	nanocontact frequency
f_{locked}	locked mode frequency
f_{PSW}	propagating spin wave frequency
f_{FMR}	ferromagnetic resonance frequency
$\Delta\varphi$	phase difference
A	exchange stiffness

List of Symbols (continued)

d_{NC}	nanocontact diameter
d_{cc}	center to center spacing
ω_b	bullet angular frequency
B_0	characteristic spin wave amplitude

List of Physical Constants

$\gamma/(2\pi)$	gyromagnetic ratio of an electron	$28.024\,\mathrm{GHz/T}$
μ_0	vacuum permeability	$4\pi \times 10^{-7}\,\mathrm{V\,s/(A\,m)}$
μ_B	Bohr magneton	$9.274 \times 10^{-24}\,\mathrm{J/T}$
e	elementary charge	$1.602 \times 10^{-19}\,\mathrm{C}$
$\hbar$	reduced Planck constant	$1.055 \times 10^{-34}\,\mathrm{J\,s}$

List of Abbreviations

CMOS	complementary metal-oxide semiconductor
STT	spin transfer torque
STNO	spin torque nano-oscillator
SHNO	spin Hall nano-oscillator
SW	spin wave
PSW	propagating spin wave
MR	magnetoresistance
GMR	giant magnetoresistance
TMR	tunneling magnetoresistance
AMR	anisotropy magnetoresistance
μ-BLS	microfocused Brillouin light scattering
dc	direct current
ac	alternating current
MTJ	magnetic tunnel junction
NP	nanopillar
NC	nanocontact
NCSTO	nanocontact spin-torque oscillator
AHE	anomalous Hall effect
SHE	spin Hall effect
SHA	spin Hall angle
LLGS	Landau–Lifshitz–Gilbert–Slonczewski
FMR	ferromagnetic resonance
LNA	low-noise amplifier
FWHM	full width at half maximum
DUT	device under test
VBW	video bandwidth
RBW	resolution bandwidth
PWVD	pseudo Wigner–Ville distribution
EBL	electron beam lithography

List of Abbreviations (continued)

SEM	scanning electron microscope
IBE	ion beam etching
SIMS	secondary ion mass spectroscopy
RIE	reactive ion etching
IP	in-plane
OOP	out-of-plane
PL	pinned layer
FL	free layer
RL	reference layer

Publications

List of papers and manuscripts included in this thesis:

I **A. Houshang**, M. Fazlali, S. R. Sani, P. Dürrenfeld, E. Iacocca, J. Åkerman, R. K. Dumas "*Effect of excitation fatigue on the synchronization of nanocontact spin-torque oscillators*", IEEE Magn. Lett. **5**, 4 (2014).

Contributions: Fabrication of the samples, Electrical measurement, and data analysis. Contributed to writing the manuscript.

II **A. Houshang**, E. Iacocca, P. Dürrenfeld, S. R. Sani, J. Åkerman, R. K. Dumas "*Spin-wave-beam driven synchronization of nanocontact spin-torque oscillators*", Nature Nanotech. **3**, 280 (2016).

Contributions: Fabrication of the samples, Electrical measurement, micromagnetic simulations, and data analysis. Contributed to writing the manuscript.

III R. K. Dumas, **A. Houshang**, J. Åkerman, "*Chapter 12 - Propagating spin waves in nano-contact spin torque oscillators*", in Spin-Wave Confinement, second edition, edited by S. Demokritov (Pan Stanford Publishing). Ch. 12 (2017).

Contributions: Fabrication of the samples, Electrical measurement, micromagnetic simulations, and data analysis. Contributed to writing the manuscript.

IV P. Dürrenfeld, A. A. Awad, **A. Houshang**, R. K. Dumas, J. Åkerman, "*A 20 nm spin Hall nano-oscillator*", Nanoscale. **9**, 1285 (2017).

Contributions: Fabrication of the samples, micromagnetic simulations, and data analysis. Contributed to writing the manuscript.

V A. A. Awad, P. Dürrenfeld, **A. Houshang**, M. Dvornik, E. Iacocca, R. K. Dumas, J. Åkerman, "*Long-range mutual synchronization of spin Hall nano-oscillators*", Nature Phys. **13**, 292 (2017).

Contributions: Fabrication of the samples, electrical measurement, and data analysis. Contributed to writing the manuscript.

VI T. Chen, R. K. Dumas, A. Eklund, P. K. Muduli, **A. Houshang**, A. A. Awad, P. Dürrenfeld, M. G. Malm, A. Rusu, J. Åkerman, "*Spin-Torque and Spin-Hall Nano-Oscillators*", Proc. IEEE **104**, 1919 (2016).

Contributions: Contributed to writing the manuscript.

VII **A. Houshang**, R. Khymyn, M. Dvornik, R. Ferreira, P. P. Freitas, R. K. Dumas, J. Åkerman, "*Evidence of solitonic and propagating spin-wave modes in hybrid magnetic tunnel junction spin-torque oscillators*", manuscript in preparation (2017).

Contributions: Fabrication of the samples, electrical measurement, and data analysis. Contributed to writing the manuscript.

List of papers related to, but not included in this thesis:

1 M. Ranjbar, P. Dürrenfeld, M. Haidar, E. Iacocca, M. Balinsky, T. Q. Le, M. Fazlali, **A. Houshang**, A. A. Awad, R. K. Dumas, J. Åkerman "*CoFeB-based spin Hall nano-oscillators*", IEEE Magn. Lett. **5**, 1 (2014).

2 H. Mazraati, S. Chung, **A. Houshang**, M. Dvornik, L. Piazza, F. Qejvanaj, S. Jiang, T. Q. Le, J. Weissenrieder, J. Åkerman, "*Low operational current spin Hall nano-oscillator based on NiFe/W bilayers*", Appl. Phys. Lett. **24**, 242402 (2016).

3 M. Zahedinejad, A. A. Awad, P. Dürrenfeld, **A. Houshang**, Y. Yin, P. K. Muduli, J. Åkerman, "*Current modulation of nanoconstriction spin Hall nano-oscillators*", IEEE Magn. Lett. **99**, 1 (2017).

Acknowledgments

First and foremost, I would honestly like to state that I am merely a spokesperson for the amazing team of researchers who have helped me to carry out the work contained in this thesis. Without their help, none of this would be possible.

Four years ago, I began a journey that turned out to be as life-changing and incredible as could be. It elevated me not, only in science, but in my personal life, and fundamentally changed how I view the world. I owe this to my main supervisor, Johan Åkerman, who granted me this opportunity. He taught me how to efficiently run and manage scientific research, and how to publish the results of that research in the best possible way. His contributions to my growth as a scientist are simply beyond words, but are not limited to that alone, because he has set many standards both in my scientific life and beyond.

I would like to thank all the senior members of our research team with whom I have enjoyed long discussions over the many scientific puzzles I faced in the course of my PhD: Ahmad Awad, Mykola Dvornik, Mohammad Haidar, Martina Ahlberg, Roman Khymyn, Sunjae Chung, and of course Fredrik Magnusson from NanOsc AB. They continuously shared their valuable insights and knowledge with me and evolved our research team to become one of the best in the world.

I would especially like to thank Philipp Dürrenfeld and Ezio Iacocca, who patiently helped me during my early days. Philipp–one of the best researchers I've ever met—taught me a lot about efficiency, patience, conducting research, and most importantly about our labs and cleanroom work. Ezio opened the door to the new world of micromagnetic simulations and patiently shared his valuable knowledge with me. Their unconditional help and support, even after they left our team, was indispensable to me. I greatly value their knowledge and friendship.

I would also like to extend my gratitude to my other team members, Shreyas Muralidhar, Hamid Mazraati, Anders Eklund, Sohrab Sani, Yuli Yin, Jinjin Yue, Tuan Le Quang, Amir Banuazizi, and Sheng Jiang. I would especially like to thank Mohammad Zahedinejad, who took on the fabrication work and helped me to focus on my thesis.

I would like to thank my PhD examiner, Raimund Feifel, and the head of Department of Physics, Mattias Goksör, for their help and support. I cannot thank the administrative staff enough, especially Bea Tensfeldt, Maria Siirak, and Clara Wilow Sundh. Their seamless support made my life much easier. The technical and machining support of Mats Rostedt and Jan-Åke Wiman

was invaluable as well.

The MC2 cleanroom facility with its top-notch equipment is where all the magic happened. It would have been impossible to do what I did without access to such a facility, and also without the support of its fantastic and professional staff, who kept the constant flow of things day in, day out. I would specifically like to thank Johan Karl Andersson, Mats Hagberg, Henrik Frederiksen, Bengt Nilsson, Marcus Rommel, Niclas Lindvall, Ulf Södervall, and Göran Alestig among many others. Your work ethics and dedication sets an example for me. A special thanks to Johan and Henrik for their table tennis lessons every now and then. I really enjoyed playing with you and I will hold on to all the nice memories.

I would like to thank all my friends outside of work who made my life in Gothenburg enjoyable and kept my balance all along the way. They brought joy and peace to my life and reminded me that there other things to life as well. Knowing that I had so many people around to help and support me, provided me with the kind of assurance everyone needs to keep going in the face of difficulties.

I consider myself to be extremely fortunate because every now and then I have come across some extraordinary people who have changed and reshaped my being to the core. Randy K. Dumas is one such person whom I had the honor to meet. His vision, intelligence, and astute comments guided me every step of the way and helped me navigate an otherwise onerous path. He is not only my cosupervisor, but my role model and, above all, my friend. I hope that some day I can be not only as good a scientist, but as good a man as he is. Words shamefully fall short so I stick to the simplest of them all: Thank you Randy, thank you for everything.

I would like to dedicate this work—which is probably the most important thing I've done in my life so far—to my family. My father and my mother have never stopped believing in and supporting me. They are always there and I am so blessed to have them by my side. They made me who I am and they are the reason behind every positive point in my life. And finally my best friend, my partner, my joy and delight, and my love, Shahrzad. You are the reason for everything that's good about me—you are the reason for it all. Your passion and your enthusiasm keep me motivated and make me want to aim for the best, side by side with you. I can only hope that I lift you up as you continue to lift me every day.

Introduction

With the ever increasing demand for high-speed and low-energy data communication, alternatives to the current complementary metal-oxide semiconductor (CMOS) systems are needed. CMOS technology is approaching its limits in terms of operation frequencies, miniaturization, and its constantly increasing power consumption. In recent years, devices based on spin, an intrinsic property of electrons, have been proposed, giving rise to a whole new research field termed *spintronics* [1, 2].

In spintronics, both the charge and the spin of carriers are taken into consideration. Spintronic devices often rely on the transfer of angular momentum from either a spin-polarized charge current or a pure spin current to a local magnetization. Spin-transfer torque (STT) was described in two seminal papers by Slonczewski [3] and Berger [4] in 1996. In these papers, it was predicted that if a large enough spin polarized current flows perpendicularly to the plane of a magnetic multilayer, the magnetization direction in one of the layers could reorient. It took only a few years for magnetization precession due to STT [5] and STT-driven magnetic switching [6] to be experimentally observed. In the following years, STT-based devices have been extensively explored and their underlying physics meticulously studied.

Some of the most interesting STT devices realized are spin torque and spin Hall nano-oscillators (STNOs and SHNOs, respectively) [5, 7–13]. Although single-layer STNOs have been demonstrated [14–16], STNOs based on all-metallic multilayers usually consist of at least two magnetic layers: one that acts primarily as a spin polarizer (the fixed layer) and another that acts as the free layer in which the spin-waves are excited. In all metallic STNOs [17–20], spin-wave (SW) dynamics are a result of multiple phenomena acting together, such as giant magnetoresistance (GMR) and STT from a spin-polarized current. However, in another class of STNOs [21–26], the free and fixed layers are separated by an insulator. In this class of devices, it is tunneling magnetoresistance (TMR) rather than GMR that comes into play. On the other hand, SHNOs [27–29] combine anisotropy magnetoresistance (AMR) with STT from a pure spin current to bring spin-wave dynamics to life. It has been shown, both experimentally and theoretically, that the STT-driven oscillations in such devices can excite dynamic states that are very different in nature, such as propagating SWs [30–32], SW bullets [33–36], and droplets [37–46].

Although all of these devices have advantages, such as high operation frequency [47–49] and modulation rates [21, 50–56], they also suffer from certain disadvantages that limit their ultimate applicability. Mutual synchronization

[57–64] has been considered a remedy to increase signal quality and power, making them potentially suitable for applications. In 2005, two seminal experiments showed that it is in fact possible to synchronize two STNOs sharing the same free layer [62, 63]. However, progress has been slow in synchronizing more than two high-frequency STNOs, and it was not until 2016 that the synchronization of SHNOs was experimentally demonstrated [65]. These developments open up many new possibilities for device layouts and their real-life applications. The simplicity of the spin-Hall-based devices facilitates optical access to regions with SW dynamics through methods such as microfocused Brillouin light scattering (μ-BLS) and time-resolved scanning Kerr microscopy (TRSKM), which both struggle with observing the magnetodynamics in STNOs where the top contact covers the most active region [12, 32, 66–68].

In the quest for devices with high power and, at the same time, narrow linewidth [69–74], another class of spintronic materials, referred to as magnetic tunnel junctions (MTJs), are also being considered. MTJs take advantage of tunneling magnetoresistance (TMR), which can be as high as 180% [75], compared to STNOs, which usually possess an MR on the order of 2% [76]. This significant difference in the MR translates into output power [77]. As a result, MTJs can yield about 6 orders of magnitude more power than STNOs [75, 78, 79]. However, MTJs have to date been based on a nanopillar (NP) geometry, in which the whole multilayer is patterned with a nanoscale cross-section. In contrast, all-metallic STNOs are typically based on a nanocontact (NC) structure (NC-STOs)—i.e., only the path through which the current enters the device is confined to the nanoscale. Although NP-MTJs can deliver high power, they also typically suffer from broad linewidths, whereas NC-STOs have reasonably narrow linewidths but fall short of MTJs in terms of power. It therefore seems logical to try and combine the best of both worlds in order to improve signal quality.

This thesis focuses on advancing the state-of-the-art devices based on spin torque and the spin Hall effect and to push the boundaries in terms of their applicability, increasing signal quality either by synchronizing many STNOs/SHNOs or fabricating hybrid structures that combine the advantages of the existing devices. The chapters are organized as follows:

Chapter 1 introduces the basics of the most important underlying physical phenomena being investigated, and describes the background required to understand the results presented in this thesis. The applied measurement techniques are introduced and are followed by subsections describing the process of fabrication for STNOs, SHNOs, and hybrid MTJs.

Chapter 2 covers STNOs based on an NC geometry. It has been shown that the Oersted field (H_{Oe}) produced by the current entering the device plays a significant role in SW propagation. The asymmetric field landscape induced by H_{Oe} results in a highly collimated and directional SW propagation pattern. By strategically defining NCs to take advantage of SW beams, the robust synchronization of five NC-STOs each separated by 300 nm is achieved—a new record. It is also demonstrated that synchronization can be stretched to greater separations of 1300 nm, consistent with the experimentally reported SW propagation length (ref). Synchronization manifests itself as an increase in

power and coherence of the synchronized mode. Furthermore, in this case, the synchronization can no longer be considered mutual in nature, but is driven by the NC from which the SWs are being propagated. Micromagnetic simulations performed by MUMAX3 confirmed the experimental results.

Chapter 3 focuses on SHNOs and studies the underlying effects that give rise to auto-oscillations. A nonmagnetic metal with high spin-orbit coupling can inject transverse spin current into an adjacent magnetic layer through the spin Hall effect. The transfer of angular momentum to the local magnetization will subsequently induce auto-oscillations. The simple bilayer structure of SHNOs makes their fabrication simpler and also provides direct optical access to the magnetically excited region. Here, only nanoconstriction SHNOs, in which both the nonmagnetic and the magnetic layers are nano-patterned, are studied. Mutual synchronization of up to nine individual constrictions separated by 300 nm was achieved. For the first time, the synchronized region was optically inspected by μ-BLS as two SW regions sharing the same spectral content.

Chapter 4 explores a new type of hybrid device based on MTJs. In order to confine the path taken by the current and force it to tunnel through the insulating barrier, MTJs are usually patterned into NPs. However, NP structures suffer from larger linewidths than NC-STOs. The larger linewidth is attributed to inhomogeneous demagnetization due to the serrated edges of the NPs and stray fields in the NP device structure. It is shown that it is possible to combine the advantages of NC structures with the high MR of MTJs into a hybrid device. STT-induced SW-modes are analyzed and their interactions are investigated in both the time and frequency domain. For the first time, experiments reveal the existence of both localized SW bullets and propagating SWs in hybrid MTJs.

Chapter 5 summarizes the results obtained in this thesis and lays out the perspectives and future works that can be explored based on the present findings.

1

Background and Methods

1.1 Theory

1.1.1 Anisotropic, Giant, and Tunneling Magnetoresistance

Anisotropic magnetoresistance (AMR)

In ferromagnetic materials, the change in electrical resistance with the relative orientation between the current flow and the magnetization direction of the medium is called anisotropic magnetoresistance (AMR) [80]. The dependence of resistance on the relative orientation of the current flow and the magnetization is described by:

$$\rho = \rho_{\perp} + (\rho_{||} - \rho_{\perp})cos^2\theta \tag{1.1}$$

here, $\rho_{\perp}$ and $\rho_{||}$ represent the resistivity of the ferromagnet when magnetization and current flow are perpendicular and parallel to each other, respectively, and θ describes an arbitrary angle between the two. AMR arises from the effect of both the magnetization and spin-orbit coupling on the charge carriers. For example, in ferromagnetic 3d alloys, the probability of s–d scattering in the magnetization direction is higher than for any other direction [81]. The AMR ratio, $(\rho_{||} - \rho_{\perp})/\rho_{\perp}$, is typically positive and can be as large as a few percent, but is typcically smaller (e.g. 0.2% for NiFe). Note that in some materials it can be negative, such as Co_2(Fe,Mn)Si Heusler alloys [82].

Giant magnetoresistance (GMR)

The discovery of GMR is responsible for the explosive growth and interest in the field of *spintronics*. GMR, the change in resistance dependent upon the relative magnetization orientation of its constituent magnetic layers, was first described by A. Fert [83] and P. Grünberg [84] in the 1980s. The most basic structure in which GMR can be detected is called a *"spin valve"*, and consists of at least two ferromagnetic layers, such as Co and NiFe, separated by a nonmagnetic conductor like Cu. While the magnetization direction of one of the magnetic layers (the *fixed layer*) is fixed, the magnetization direction of the

other magnetic layer (the *free layer*) can be changed at relatively small fields. GMR arises due to the spin-dependent scattering of electrons when passing through or scattering off of ferromagnetic layers and can be explained by the Mott model [85]. GMR has the highest value when the magnetization direction of the fixed and free layer are antiparallel. In this case, both the up-spin and down-spin electrons are strongly scattered by the two magnetic layers, producing a high-resistance state. On the other hand, when the magnetization direction of the fixed and free layer are parallel, electrons with a certain spin direction will be scattered, while the other type experiences little scattering, resulting in a lower-resistance state. The greater the GMR effect, the higher the magnetoresistance (MR) ratio. The GMR ratio is defined as:

$$GMR = \frac{R_{AP} - R_P}{R_P} = \frac{\Delta R}{R_P}, \tag{1.2}$$

where R_{AP} and R_P are the resistance of the spin valve structure when the magnetization direction of the fixed and free layer are antiparallel and parallel, respectively.

Tunneling magnetoresistance (TMR)

The layer structure for TMR is similar to that of GMR, with one important distinction. In magnetic tunnel junctions (MTJs), an ultrathin *insulating* layer separates the ferromagnetic layers from each other (in this case, they are called the reference layer and the free layer). Electrons can tunnel through the thin insulating layer; the probability of tunneling depends on the relative magnetization direction of the adjacent ferromagnetic layers. Here again, when the magnetization orientation of the free and reference layers are parallel, the resistance is lower than the state in which the layers are oriented antiparallel to each other. The TMR ratio can describe the change in resistance over the MTJ:

$$TMR = \frac{2P_1P_2}{1 - P_1P_2}, \tag{1.3}$$

P_1 and P_2 are the spin polarization of the ferromagnetic layers. P_i is defined as:

$$P_i = \frac{D_{i\uparrow} - Di\downarrow}{D_{i\uparrow} + Di\downarrow}; i = 1, 2 \tag{1.4}$$

$D_{i\uparrow}$ and $D_{i\downarrow}$ are the density of up-spin and down-spin electrons at the Fermi energy level of the ferromagnet. While the GMR ratio is on the order of a few percent (1%–2%) [76], TMR ratios exceeding 150% have been reported in the literature [75, 79, 86].

1.1.2 Spin Hall Effect

When current passes through a conductor that is subject to a magnetic field perpendicular to the current flow, a potential difference is generated across

it. This effect was first discovered by E. H. Hall in 1879 [87]. Soon after, it was also found that the current flow in a ferromagnet acquires a net polarization which is determined by the magnetization direction of the medium [88]. Such a current experiences a transverse velocity with different paths for electrons with different spin orientations, and eventually produces a transverse voltage. This phenomenon is called the anomalous Hall effect (AHE)[88, 89]. The spin Hall effect (SHE) shares the same concept as AHE, but is limited to nonmagnetic materials, with an important distinction: a current passing through a nonmagnetic material will not become polarized, and therefore the spin-dependent charge separation will not yield a measurable voltage—that is, there is no spin imbalance in a nonmagnetic material. The SHE manifests itself as a spin current transverse to the charge current and eventually results in spins with opposite polarities accumulating at opposite faces of the nonmagnetic conductor [90–94].

The SHE may be due to either intrinsic or extrinsic mechanisms. Intrinsic mechanisms occur because of the effect of spin-orbit coupling on the band structure of the metal, which exerts a force on electrons between scattering events [95]. However, Extrinsic mechanisms, such as side-jump [96] and spin skew scattering [97] rely on scattering events, which depend on impurities in the materials.

The spin Hall angle (SHA), θ_{SH}, quantifies the conversion efficiency between charge current and pure spin current, and can be calculated from the following [91]:

$$\theta_{SH} = \frac{\sigma^s_{xy}}{\sigma^c_{xx}} \frac{e}{\hbar}, \tag{1.5}$$

where σ^s_{xy} and σ^c_{xx} are the spin Hall conductivity and charge conductivity, respectively. SHA is usually reported as a percentage and may be either positive or negative depending on the material. As an example, metals like Ta and W, with less than half-filled d-orbitals, have negative SHAs, while Pt and Pd, with more than half-filled d-orbitals, show positive SHAs. A model that only considers the intrinsic spin Hall effect has been proposed for 4d and 5d transition metals and has been shown to explain their measured SHAs [98–100].

1.1.3 Spin Transfer Torque

Magnetization dynamics in our devices can be, to a large degree, described classically by the Landau–Lifshitz–Gilbert equation [101] with an additional term to describe the spin-torque effect on magnetization dynamics, first introduced by Slonczewski [3] and Berger [4]. The Landau–Lifshitz–Gilbert–Slonczewski (LLGS) equation is as follows:

$$\frac{\partial \vec{M}}{\partial t} = -\gamma(\vec{M} \times \vec{H}_{eff}) - \frac{\gamma\alpha}{M_0}[\vec{M} \times (\vec{M} \times \vec{H}_{eff})] + \tau[\vec{M} \times (\vec{M} \times \vec{P})], \tag{1.6}$$

where $\vec{M}$ is the magnetization vector, $\vec{H}_{eff}$ is the effective field, γ is the gyromagnetic ratio, α is the Gilbert damping constant, and $\vec{P}$ is a vector

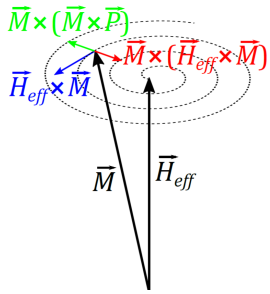

Figure 1.1: Schematic representation of LLGS equation. The blue term (the first in the LLGS equation) is a conservative torque and causes precession around $\vec{H}_{eff}$. The red (second) term describes the dissipative torque, which results in the spiral motion of $\vec{M}$ shown by the black dashed line. Finally, the green (third) term is the spin-transfer torque which, when sufficiently large, can compensate for the damping term and cause steady-state precession.

pointing in the spin polarization direction of the bias current. $\vec{H}_{eff}$ itself is the sum of the external magnetic field $\vec{H}_{ext}$, the magnetodipolar field $\vec{H}_{dip}$, the exchange field $\vec{H}_{ex}$, the anisotropy field $\vec{H}_A$, and the Oersted magnetic field $\vec{H}_I$ produced by the current going through the device. The first term on the right-hand side of Equation 1.1 describes the undamped conservative precession of $\vec{M}$; The second term on the right-hand side or Equation 1.1 represents the damping of the medium and causes the $\vec{M}$ to finally align with $\vec{H}_{eff}$. The final term on the right-hand side of Equation 1.1 represents the Slonczewski–Berger torque or spin-transfer torque (STT), and provides an antidamping torque that, when sufficiently large, can overcome the natural damping of the medium and lead to the steady-state precession of $\vec{M}$. The direction of these three terms is color coded in Figure 1.1.

The spin-polarized current needed for STT to occur can come from a number of sources. In one of the cases covered in this thesis, a spin-valve structure produces the spin-polarized current. When a current goes through a ferromagnetic layer, it becomes polarized. Depending on the polarization direction of this current, it could exert a torque on the free layer, which can be described by Equation 1.1. Another mechanism for producing a spin-polarized current is the spin Hall effect, which was briefly reviewed earlier.

1.1.4 Spin Torque Nano-Oscillators (STNOs)

STT-induced magnetization dynamics can only be obtained at high current densities, on the order of $10^{12} A/m^2$. Such high current densities can only be achieved if the cross-section of the current path is confined to nanoscale dimensions. A schematic of such a device is shown in Figure 1.2. In this thesis, we only focus on nanocontacts, nanoconstrictions, and hybrid geometries, as shown in Figures 1.2(b–d).

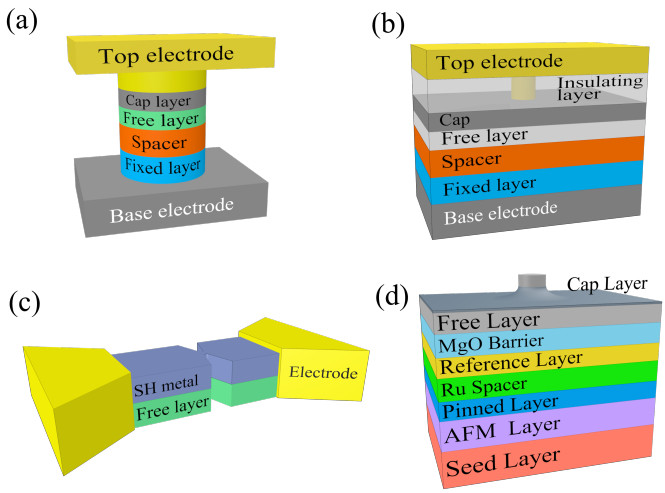

Figure 1.2: Schematic illustration of different types of STNOs. (a) Nanopillar, (b) Nanocontact, (c) Nanoconstriction, and (d) Hybrid geometries.

Nanocontact geometry

In the nanocontact (NC) geometry, only the path through which the current enters the device is confined, as can be seen in Figure 1.2(b). The nanocontact spin-torque oscillators (NCSTOs) studied in this thesis are in the range of 90 to 100 nm in size. The dimensions of the spin-valve mesa in which these NCs are fabricated is $8 \times 16 \mu m^2$, and can be considered essentially infinite with respect to the NCs. This geometry allows multiple NCs sharing the same free layer to be fabricated.

Nanoconstriction geometry

Nanoconstriction geometry is used for the spin Hall nano-oscillators (SHNOs). As can be seen in Figure 1.2(c), a bow-tie shaped constriction is designed to confine the current. The flow of in-plane current will produce spin accumulation at the lateral surfaces of the metal, one of which is the interface between the metal and the ferromagnet in bilayer SHNOs [18]. This specific structure has some advantages over the nanocontact geometry, including easier nanofabrication process and direct optical access to the magnetically dynamic area [65].

Hybrid geometry

Typically, MTJs are fabricated utilizing a nanopillar geometry (Fig. 1.2(a)), however, these structures are not only very hard to fabricate but also affect device performance and introduce inhomogeneity to the structure [102–105]. The nanocontact geometry cannot be used for MTJs, since most of the current will stray into the cap layer and therefore fail to contribute to the magnetization

dynamics. Considering all the advantages of the nanocontact geometry and disadvantages of the nanopillar structure, a hybrid geometry that combines the benefits of both structures was designed and its basic functionality were studied [106, 107]. Figure 1.2 (d) schematically illustrates such a device.

Achieving a high current density is a necessary but not a sufficient step towards realizing magnetization dynamics. The initiation of magnetization dynamics depends on current direction as well. Electrons flowing from the fixed to the free layer carry the fixed-layer polarization direction. In this case, the spin torque transferred from the electrons, will assist the Gilbert damping in making the magnetization of the free and fixed layers parallel. However, when the current is directed such that the electrons flow from the free to the fixed layer, the angular momentum transferred will act to orient the fixed layer along the direction of the free layer. Since the magnetization direction of the fixed layer does not change easily, this effect is negligible. However, in this case, electrons having an antiparallel spin angular momentum with the fixed layer will back-scatter from the interface between the spacer and the fixed layer. This time, when these electrons enter the free layer, will act in opposition to the Gilbert damping and thus sustain auto-oscillations.

1.1.5 Magnetization dynamics in STNOs

Magnetization precession in a ferromagnet can give rise to different states and modes with completely different characteristics. The key concept in understanding the nature of these modes is *spin waves* (SWs). At T=0 K, all the spins in a ferromagnet are aligned parallel to each other, and the magnetization of the material is at its maximum. When the temperature increases, spins begin to tilt with respect to each other. Since spins interact with each other through the exchange interaction, the tilting of each of them affects the neighboring spins, making them tilt as well. Eventually, they will have aligned as shown in Figure 1.3; looking at this, it can be seen why this alignment is referred to as a spin wave. Another key concept that plays a vital role in understanding the nature of the SW modes in STNOs is *ferromagnetic resonance* (FMR), which is the collective motion of the magnetization vectors (k=0) in a ferromagnet about an external magnetic field. The FMR frequency for a magnetized thin film can be obtained from:

$$f_{FMR} = \frac{\gamma \mu_0}{2\pi} \sqrt{H_{int}(H_{int} + M_0 cos^2 \theta_{int})}, \tag{1.7}$$

in which H_{int} and θ_{int} are the internal field and angle, and can be obtained by solving the magnetostatic boundary conditions:

$$\begin{aligned} H_{ext}\ \cos\theta_{ext} &= H_{int}\ \cos\theta_{int}, \\ H_{ext}\ \sin\theta_{ext} &= (H_{int} + M_0)\sin\theta_{int}. \end{aligned} \tag{1.8}$$

The well-known Kittel equation for in-plane magnetized thin films is a special case of Equation 1.7 when $\theta_{int} = 0$ [108–110].

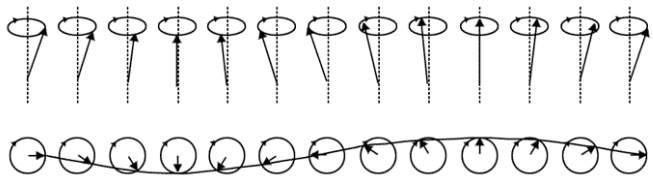

Figure 1.3: Schematic of a 1-D alignment of spins at a nonzero temperature.

Depending on the anisotropy of the ferromagnetic layers in the STNO devices mentioned in the previous section, different types of SW modes can form. In this thesis, only devices with in-plane anisotropy are investigated. In this type of devices, current injection gives rise to essentially two different SW modes: the "*propagating*" SW mode [30] and the localized solitonic "*bullet*" mode [33].

Propagating spin wave mode

This was the first mode that was predicted to be excited in NCSTOs [30]. It was argued that, at currents above a threshold value, dynamics under the NC could be established for a perpendicularly magnetized free layer like NiFe. The magnetization precesses with a larger cone angle compared with FMR, and so increases the internal field. As a result, the generation frequency of the magnetization dynamics is higher than with FMR. The same result can also be obtained from the theoretical framework developed by Slavin *et al.* [101], who also predicted that the propagating SW mode is the only stable mode at external field angles above a critical value, θ_c. For example, for the NCSTOs studied in this thesis, $\theta_c \approx 60°$. Another important observation made in the case of propagating SWs results from the fact that the free layer is infinite with respect to the NC in two of the three dimensions, and so the magnetization dynamics couples to the surrounding spins through the exchange interaction. As a result, the generated dynamics propagates away from the NC radially, as shown schematically in Figure 1.4(a). This prediction was later optically observed by a method called micro-focused Brillouin light scattering (μ-focused BLS) [32]. This result has far-reaching consequences, as will be shown later in this thesis.

Localized bullet mode

In addition to the propagating SW mode, Slavin and Tiberkevich [33] showed that for external field angles less than θ_c, another mode—the bullet mode—can also be nucleated [31, 35]. The frequency of this self-localized solitonic mode is less than FMR because of a negative nonlinearity coefficient. This mode comes into existence only when the energy of the system reaches a minimum, and so less current is needed to nucleate the bullet mode than the propagating mode for the same conditions. Figure 1.4(b) illustrates a spin-wave bullet schematically.

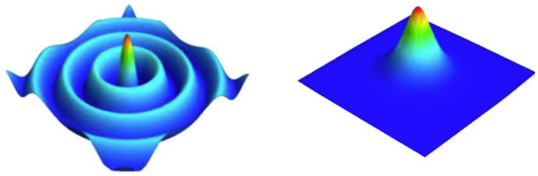

Figure 1.4: (a) Propagating spin wave mode, (b) spin wave bullet.

1.1.6 Synchronization Phenomena

Synchronization is defined as the "adjustment of the rhythm of oscillating objects due to their weak interaction" and it is considered to be natural phenomena in nonlinear coupled oscillators [111]. Mutual synchronization has been realized for NCSTOs sharing the same free layer and has been shown to improve the signal quality by increasing the output power and decreasing the linewidth of the synchronized state [62–64, 112]. Synchronization increases the mode volume, making it less susceptible to thermal fluctuations and thus increasing (decreasing) the mode uniformity (linewidth) of the final state. In all the cases studied in the literature, synchronization is said to be "mutual", because it is believed that all the oscillators play the same active role in the final synchronized state. Synchronization is attributed to different mechanisms, the most important of which is through propagating SWs [112]. It is, therefore, crucial to study all the factors affecting SW propagation pattern.

1.2 Experimental Methods

1.2.1 Electrical Measurement

The characterization of the devices fabricated in this thesis was carried out through their microwave signal generation, which was induced as a result of current-induced STT-driven precession of their magnetization. This precession results in a time-varying resistance change (in the GHz range) and manifests itself as an AC voltage signal, which is decoupled from the applied DC current using a broadband bias tee. Since the power of the signals generated by the devices studied in this thesis is usually low—below the noise floor of the spectrum analyzer—a low-noise amplifier with a gain of ≥ 32 dB and a noise figure of ≤ 3 dB is used to raise the power. The amplified signals are then sent to a Rhode & Schwarz FSV-40 spectrum analyzer with the video bandwidth (VBW) and the resolution bandwidth (RBW) set to 10 KHz and 1 MHz, respectively. A Keithley 2400 source-measure unit is used to provide the dc current and to measure the resistance of the devices. The results were analyzed in the MATLAB programming environment. They are corrected for their amplifier gain and their losses caused as a result of the impedance mismatch of the rf circuit (with a fixed 50 Ω impedance) and the device under test (DUT). The signals obtained are then fitted with a symmetric Lorentzian function, from

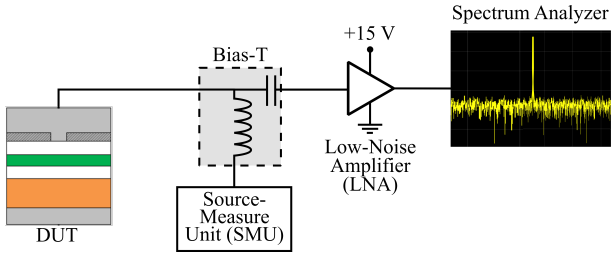

Figure 1.5: Schematic of an electrical measurement setup used for microwave detection of magnetization dynamics in the devices. A dc current is applied to the device under test (DUT). The microwave response is decoupled by the bias-T and is amplified by the LNA before being recorded by the spectrum analyzer. The resulting spectra is later fitted by a Lorentzian function to extract integrated power and FWHM linewidth.

which the signal frequency, integrated power, and full-width-at-half-maximum (FWHM) linewidths can be obtained.

Measurements in the time-domain was performed using a LeCroy WaveMaster 8 Zi-B digital oscilloscope with a 30 GHz bandwidth and 80 GH/s sampling rate. 10 μs-long single-shot time traces with self-triggered signals were captured and amplified before being recorded by the oscilloscope. A fast Fourier transform (FFT) was performed on the time traces to obtain the signal frequency. The time traces were further analyzed by a pseudo-Wigner–Ville distribution (PWVD) function with time (frequency) resolution of 2 ns (0.5 GHz).

1.2.2 Microfocused Brillouin Light Scattering (μ-focused BLS)

In this thesis, SHNOs were investigated by μ-focused BLS using a 532 nm single-frequency laser provided by a single diode-pumped solid-state laser. The laser spot is focused in the range of diffraction limit using dark-field Zeiss objectives with a numerical aperture NA = 0.75. Spatial maps are obtained by scanning the sample underneath the laser spot. The scattered light is then analyzed using a six-pass Tandem Fabry–Perot TFP-1 interferometer, which is the most important part of the setup and should possess a high frequency resolution to distinguish different SW modes. A single photon counter records the frequency-resolved intensities on the measurement computer. This intensity is proportional to the square root of the magnetization dynamics amplitude at that specific frequency. BLS provides the unique opportunity of giving direct access to the spin waves and magnetization dynamics in SHNOs. The underlying mechanism in this method is through the interaction of quanta of light (photons) and quanta of SWs (magnons). When the laser hits an FM film, it may either create or annihilate magnons and thereby gain or lose energy. The change in energy will eventually cause a shift in both the wavelength and

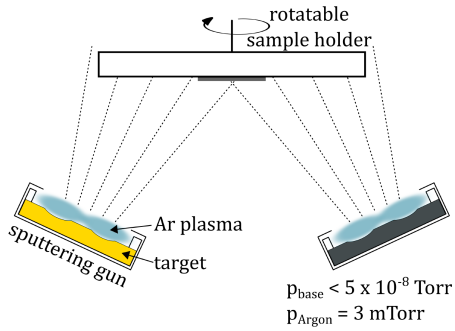

Figure 1.6: Schematic of the sputtering system used for thin film deposition. Each gun has a shutter, which is not shown. The rotatable sample holder and the confocal arrangement of the guns ensure a uniform thickness of the deposited films throughout the entire sample [114].

frequency of the scattered light. This shift is detected and analyzed by the interferometer.

1.3 Fabrication

1.3.1 Fabrication of Nanoconstriction SHNOs

A detailed fabrication process for NC-STOs and needle-based SHNOs has previously been developed in our team [113, 114]. In this thesis, the detailed process for fabricating nanoconstrictions and hybrid MTJs is explained. There were many challenges in the fabrication process of these devices (especially for hybrid MTJs), and many process parameters had to be optimized to yield the desired result.

Thin film deposition

Deposition of films are done in an AJA Phase II system containing seven confocal sputtering targets in a circular arrangement within a high vacuum chamber. The chamber base pressure is lower than 5×10^{-8} Torr. Sputtering is done at 3 mTorr of Ar pressure. The confocal arrangement of the guns and the rotatable sample holder ensure the greatest uniformity at 40 mm working distance, which is the distance between the sample and the plane in which the guns are located. An 18 mm×18 mm, c-plane Al_2O_3 substrate is transferred to the main sputtering chamber via a load-lock in which, first, 5 nm of NiFe and, immediately after that, 6 nm of Pt is sputtered on it. Figure 1.6, adapted from [114], schematically show the sputtering targets and the position of the sample holder with respect to them.

Alignment mark fabrication

The choice of the alignment mark material depends on the electron beam lithography (EBL) system and how it performs mark detection. In the EBL system used in this thesis, the alignment mark is detected by the change in the secondary electrons when the electron beam is scanning the substrate and passes over the leg of the alignment cross. The contrast between the substrate and the alignment mark increases with the thickness of the mark, and also depends on the difference between the atomic number of the substrate and the alignment mark material. It was thus decided to sputter a 100 nm thick layer of tantalum, which has a high atomic number (Z=73) and good adhesion to the sapphire substrate. Photolithography combined with a lift-off process is used to define the marks. The resist combination used for the lift-off process is a 100 nm thick MicroChem LOR 1A lift-off spacer together with a 1.3-μm-thick S1813 photoresist. Exposure is done using a Heidelberg Instruments DWL 2000 laser writer that uses a diode laser with a wavelength of 405 nm to expose the resist. Since the lift-off layer develops faster than the photoresist, it leaves an undercut behind. Tantalum is then sputtered on the resist bilayer and is left in a hot bath of photoresist remover for lift-off.

Fabrication of nanoconstrictions

Nanoconstriction SHNOs are patterned so that the current is focused by their shape (Fig. 1.2(c)), similarly to nanopillar MTJ devices, in which the whole device is patterned in nanodimensions (Fig. 1.2(a)). The need for a high level of control over the lateral dimensions of nanoconstriction and the fact that a noble metal, Pt, is used in the SHNO material stack rules out the possibility of chemical wet etching and leaves physical ion beam etching (IBE) as the best option. IBE is performed by bombardment with Ar noble gas. It thus has no material selectivity. This makes it possible to use a negative-tone e-beam resist as the etching mask, as long as the thickness of the resist is larger than the material stack being etched. IBE is normally carried out at 25° which is the angle between the normal to the sample surface and the bombardment direction, to avoid sidewall buildup in the ion milling process. One can also change the IBE angle to achieve precise control over the lateral dimensions of the constriction. Increasing the milling angle will increase the etching rate in the lateral dimensions and subsequently the lateral dimensions can be reduced to the desired level. Etching of each layer is carefully controlled by an in situ secondary ion mass spectroscopy (SIMS) endpoint detection. Figure 1.6 shows schematics of different steps involved in the fabrication of SHNOs and a scanning electron microscope image of a final device, Figure 1.6(e). After pattern transfer is done, a reactive ion etching (RIE) plasma system is used for oxygen cleaning and removing the resist residual, followed by resting the samples in hot resist removal bath to remove any remaining resist.

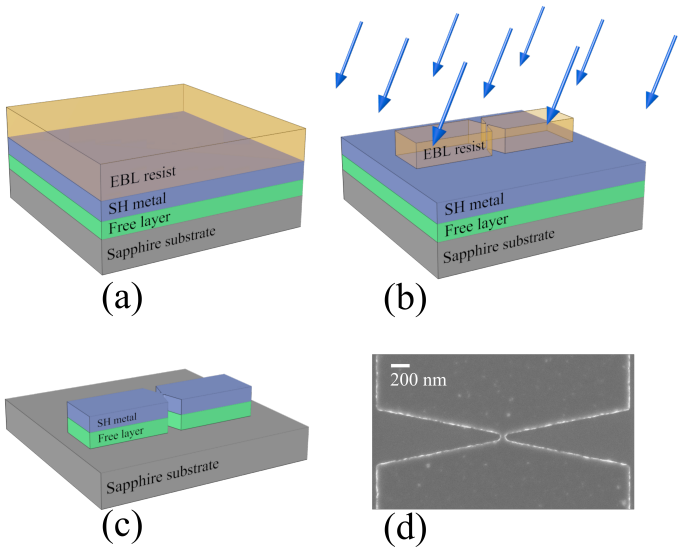

Figure 1.7: (a) Ma-N 2401 negative tone EBL resist is spin-coated on the sample; (b) after EBL exposure and development, the resist is used as an etching mask for IBE at an angle of 25°. (d) By removing the remaining resist, pattern transfer to the blank films is complete (e) SEM image of a 100 nm nanoconstriction device.

1.3.2 Fabrication of Hybrid MTJ

The final goal for hybrid MTJs is to thin down the cap layers (here ruthenium and tantalum) as much as possible, so that stray current is reduced and the current is instead forced through the layers. The final structure therefore has the unique shape shown in Figure 1.2(d): it is neither like a nanopillar whose whole structure is patterned in nanodimensions nor like an NC structure in which only the path through which the current enters the device has nanodimensions.

The mesa fabrication step is similar to mesa fabrication for NCSTOs, which was previously developed in our team [113, 114]. To make the hybrid structure, a negative tone resist is used again as an etching mask for an IBE process. Taking advantage of the in situ SIMS, etching down the cap layer is carefully controlled to prevent any damage to the layers beneath the cap. After the etching, while still keeping the resist, 30 nm of SiO_2 is deposited to act as an insulating barrier between the cap and the top contact. The devices are left in a hot bath of remover placed in a high-energy ultrasonic machine. The same resist layer that was used as an etching mask now acts as a lift-off layer. The process steps in fabricating hybrid MTJs is illustrated in Figure 1.7(a–d).

Top contact fabrication

Top contact waveguides are fabricated to provide electrical access to the devices. The top contact signal and ground pads are 100 μm wide to facilitate microwave

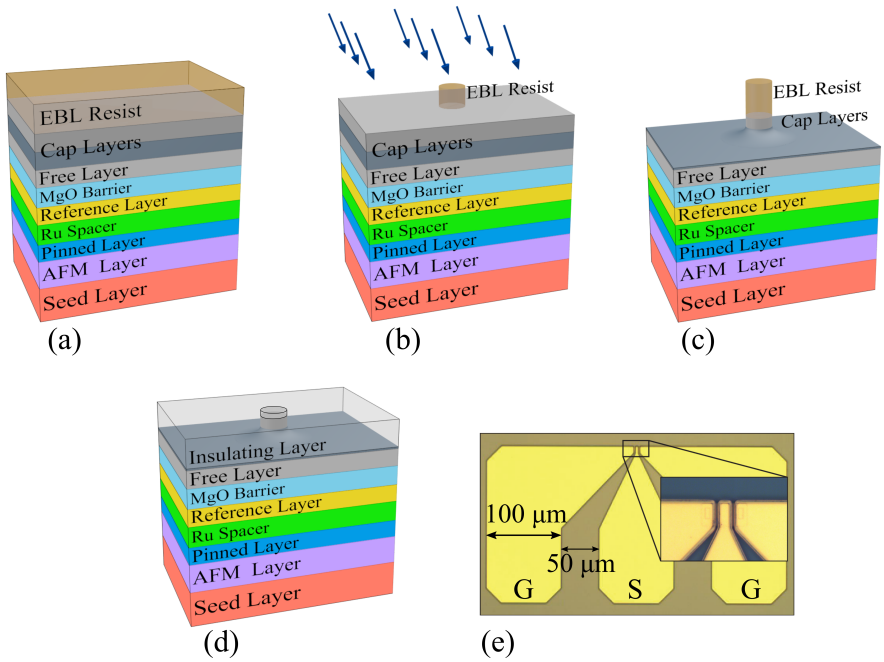

Figure 1.8: (a) Ma-N 2401 negative tone EBL resist is spin-coated on the sample; (b) after EBL exposure and development, IBE is carried out at 45° using the EBL resist as an etching mask; (c) cap layer shape after IBE. The remaining resist is used as a lift-off layer for the insulating barrier; (d) after depositing SiO_2 and performing lift-off, the top contact can be fabricated to provide electrical access to the device; (e) optical image of a waveguide that provides electrical access to the devices; "G" and "S" refer to the ground and signal legs of the microwave probe.

probe contact. The gaps between the signal and ground strips are designed in such a way that their width is half of the signal strip's (Fig. 1.7(e)). This will lead to a rf impedance of about 50 Ω [76], which provides good matching with the impedance of the circuit. Top contacts are defined by photolithography and through a lift-off process, as previously explained. However, instead of using LOR 1A, a 500-nm-thick LOR 3A lift-off resist is used, which yields a clean-cut lift-off of 1-μm-thick Cu waveguides.

2

Nanocontact Spin-Torque Oscillators (NCSTOs)

Magnetization dynamics in GMR-based NCSTOs based on all in-plane [4, 7, 8, 31, 34, 36, 115], all perpendicular [116, 117], orthogonal [38, 39, 44, 118–121], and tilted magnetic layers [122–131], has been extensively studied. In this thesis, the focus is on the nanocontacts in which the equilibrium magnetization of both the free and the fixed layer lie in-plane. In this type of device, the nature of the excited mode strongly depends on the external magnetic field direction as shown in [36]. It has been shown analytically [33] and through micromagnetic simulations [132–134] that the mode excited in an in-plane external field excites a self-localized solitonic bullet mode [8, 31]. However, when the external field is applied perpendicular to the plane of the film, an exchange dominated propagating mode is excited [30]. BLS shows the wavevector of the excited mode to be inversely proportional to the NC radius [32]. At intermediate angles, simulations [31, 135] and experiments [104] suggest that the mode hops between the bullet and the propagating mode [9, 72, 136].

Mutual synchronization has been proposed as a means to achieve sufficient signal quality for applications. However, since the early papers showing mutual synchronization of two NCSTOs sharing the same free layer [62, 63], progress has been slow on synchronizing more oscillators, and it was not until 2013 that the mutual synchronization of three NCSTOs was reported [64].

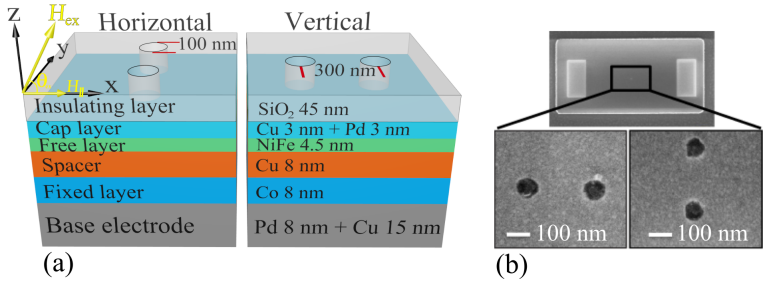

Figure 2.1: (a) Schematic of horizontal and vertical geometries. Device geometry is defined with respect to $H_{||}$, (b) SEM images of horizontal and vertical NC geometries with 100 nm nominal diameter.

2.1 Synchronization and Oersted Field

In all the above-mentioned cases, synchronization was promoted by propagating SWs. It thus seems crucial to study the factors that affect SW propagation patterns. The current-induced Oersted field not only localizes the SW modes but also promotes an asymmetric magnetic field landscape, which locally modifies the FMR frequency [137], making SWs propagate into the low-field (low-FMR) region. When the SW frequency is lower than the local FMR frequency, propagation is hampered, and the so-called Corral effect [138] results in highly collimated SW beams.

2.2 Device Geometries

To show the importance of SWs in the synchronization of NCSTOs, two different NC geometries are considered—see Fig. 2.1(a). The horizontal and vertical geometries are defined based on the in-plane component of the external magnetic field, $H_{||}$ which, as can be seen in Figure 2-1(a), points to the positive x-axis. NCs are defined on top of a pseudo-spin-valve mesa, details of which are shown in Figure 2-1(a). The nominal diameter of the NCs is 100 nm with a center-to-center (cc) separation of 300 nm. Figure 2-1(b) shows SEM images of the final devices. Experimental results on both of these geometries are presented in the following, together with a meticulous study of the FMR landscape. The SW propagation pattern in each case is simulated by MUMAX3 [139].

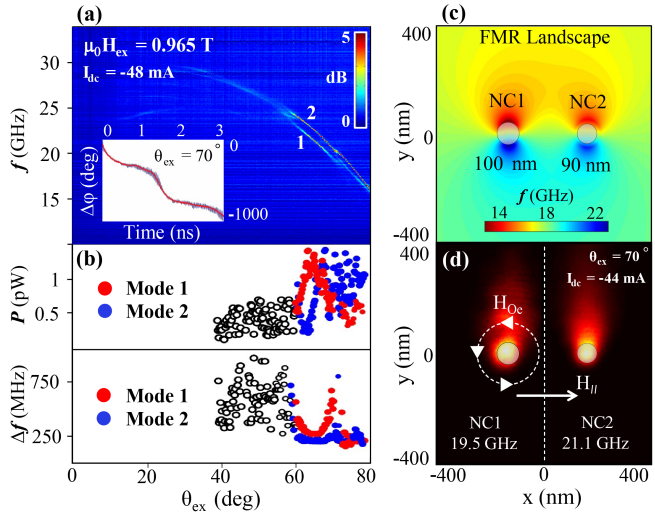

Figure 2.2: (a) Experimental frequency response of two horizontal NCs with a nominal diameter of 100 nm and cc spacing of 300 nm for $\mu_0 H_{ex}$ = 0.965 T and I_{dc}= -48 mA, measured as a function of θ_{ex}. The inset shows the simulated phase difference between the NCs, which indicates the NCs are not synchronized; (b) integrated power and linewidth of the experimental results for mode 1 and 2 denoted with solid red and blue circles, respectively. The open circles correspond to the modes seen at angles below θ_c; (c) FMR landscape calculated using the Kittel equation and solving the magnetostatic boundary conditions by taking both θ_{ex} and θ_{Oe} into account; (d) simulated spatial profile of SW propagation pattern from two NCs in a horizontal geometry for $\mu_0 H_{ex}$ = 0.965 T and I_{dc}= -44 mA, showing collimated SW beams.

2.2.1 Horizontal Geometry

To gain a better understanding of SW propagation, experiments were conducted similar to those from 2005 in [62, 63]. The result for the experimental frequency response of the NCs as a function of external field angle, θ_{ex}, with I_{dc}= -44 mA is shown in Figure 2.2(a). As was previously mentioned , when θ_{ex} is larger than a critical angle, $\theta_c = 60°$, a single propagating mode [32] is observed. Here, two propagating modes with different frequencies are observed, labeled mode 1 and 2, which indicates that the NCs are not synchronized in this geometry and at the mentioned current. The integrated power P and linewidth Δf of each of the modes are shown in Figure 2.2(b) with solid red and blue circles. The micromagnetically simulated phase difference $\Delta\varphi$ between NCs also shows a monotonic decrease as a function of time, indicating that synchronization is not achieved for $\theta_{ex} = 70°$. At I_{dc}= -44 mA, the Oersted field, H_{Oe}, is about 10% of the external magnetic field, H_{ex}, and therefore significantly changes the total field in the vicinity of the NCs. Since electrons flow into the page, the local field maximum is at the bottom of the NCs, where both θ_{ex} and θ_{Oe} point

in the same direction. However, on top of the NCs, the local field is minimum because θ_{ex} and θ_{ex} point opposite to each other. Having a field landscape allows us to define the FMR frequency locally through the Kittel equation and to solve the magnetostatic boundary conditions for $\theta_{ex} = 70°$. Figure 2.2(c) shows the resulting calculated FMR frequency landscape. SWs with a frequency higher than that of the local FMR frequency can easily propagate to the far field [138], which are the regions above the NCs, as shown in Figure 2.2(c), producing highly collimated SW beams. Simulations corroborate this picture. The spatial profile of each mode obtained by performing FFT on each simulation cell and filtering the obtained image around a given frequency is shown in Figure 2.2(d). Two distinct modes with different frequencies can be assigned to each of the NCs with f_{NC1}=19.5 GHz and f_{NC2}=21.1 GHz. The color intensity of the linear maps is proportional to the power of the modes. It is obvious that the majority of SW energy emitted from each NC propagates away from the other, which hampers mutual synchronization. It must be stated that, in the horizontal geometry too, NCs sometimes become synchronized, but the probability of synchronization is on the order of a few percent [62].

2.2.2 Vertical Geometry

When the geometry of the NCs is changed to vertical, a different behavior is experimentally observed. As can be seen in Figure 2.3(a), for $\theta_{ex} > 60°$ there are two modes labeled 1+2 and X with a frequency difference of about 3 GHz. The behavior of the integrated power and linewidth is quite different from in the horizontal geometry. The integrated power (linewidth) of the 1+2 mode is much larger (smaller) than for either of the modes observed in the horizontal geometry, which is consistent with a synchronized state. The difference between the horizontal and vertical geometry becomes more apparent when the behavior of the device with vertical geometry is investigated as a function of the current at a fixed external angle, $\theta_{ex} = 70°$, as shown in Figure 2.3(c). Mode 1+2 shows blue shifting as the current is increased, which is consistent with the behavior of propagating SWs in similar experiments [31, 53, 62]. Furthermore, a single 1+2 mode is observed for the entire current range, showing robust synchronization. Simulation also shows that the phase difference between the NCs, $\Delta\varphi$, converges to a constant value, indicating that the NCs are synchronized or phase-locked. However, the frequency of mode X is almost constant as a function of current. The magnetic field and the consequent FMR frequency landscapes are completely different in the vertical geometry, as can be seen in Figure 2.4(a). As the SWs propagate upwards, this geometry is preferred for communication between the NCs. The situation becomes more apparent when a single line scan of the FMR landscape is plotted along x=0 nm. This plot is shown by the solid blue line in Figure 2.4(b). As can be seen, the simulated locked mode frequency, $f_{locked} = 20.51$ GHz, lies above the local FMR frequency (bold green line) in the region between the NCs (gray regions).

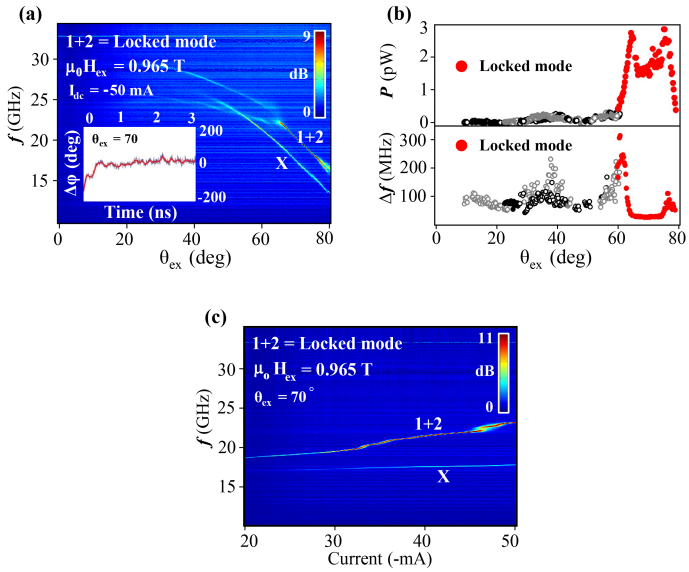

Figure 2.3: (a) Experimental frequency response of two vertical NCs with a nominal diameter of 100 nm and cc spacing of 300 nm for $\mu_0 H_{ex} = 0.965$ T and I_{dc}= -44 mA measured as a function of θ_{ex}. The inset shows the simulated phase difference between the NCs. A constant phase difference is an indication of synchronization or phase locking of the NCs. (b) Integrated power and linewidth of the 1+2 locked mode, solid red circles as a function of θ_{ex}. The open symbols correspond to the localized mode at lower θ_{ex}. (c) Experimental frequency spectra as a function of I_{dc}, showing that the locked 1+2 mode blueshifts in frequency while the X mode frequency remains almost constant over the entire current range, suggesting a different origin.

The simulated spatial map of the locked mode, Figure 2.4(c), reveals that power intensity is highest underneath the NCs. Furthermore, by taking advantage of a stepwise simulation, as shown in Figure 2.4(e), the mechanism of synchronization can be further elucidated. Simulations are performed in such a way that, although current runs through the NCs so that the FMR landscape is preserved, the spin polarization p is individually controlled at a time. This is done so that the natural frequency of each NC can be determined. In the first step, when $p_{NC1} = 0.3$ and $p_{NC1} = 0$, the natural frequency of NC1, f_{NC1}, is found to be 20.48 GHz. Similarly, f_{NC2} is found to be 21.1 GHz, as shown in Fig 2.4(e). Finally, when both NCs are turned on, the frequency of the locked mode is 20.5 GHz, which is very close to the frequency of NC1—that is, the NC from which the SWs are emitted. This simple simulation reveals that the lower NC plays the dominant role. Therefore, the synchronization can no longer be said to be mutual, but is rather *driven* by the lower NC.

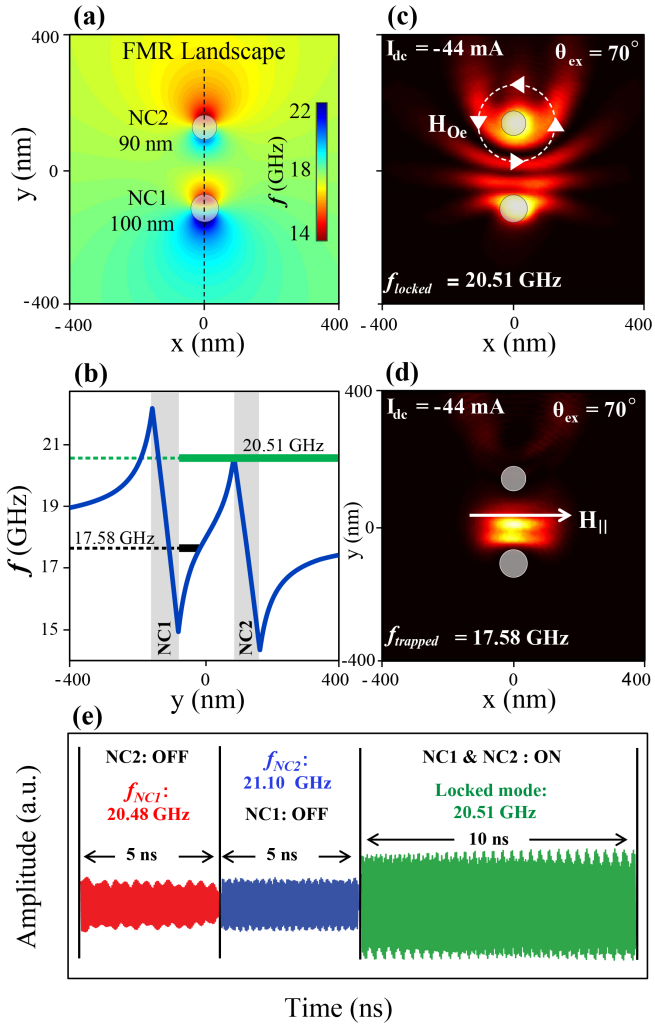

Figure 2.4: (a) Two-dimensional FMR frequency landscape. (b) FMR frequency along x=0 nm. The bold green line is the frequency of the simulated locked mode and the bold black line is the simulated trapped mode frequency. (c) and (d) are the spatial distributions of the locked and trapped mode, respectively. (d) Simulations in which first NC1, then NC2, and finally both NCs are turned on.

The spatial map of the X mode, Figure 2.4(d), reveals that it is localized in a region just outside the lower NC due to the unique local FMR landscape (Figure 2.4(b)); for this reason it is called the 'trapped mode'. This mode appears in simulations and experiments only for the vertical geometry. It can be argued that the H_{Oe} landscape creates such a local field minimum outside NC1 (Figure 2.4(b)), similar to that generated by a magnetic tip in an adjacent

magnetic film in scanning probe FMR measurements [140]. Assuming that the local field minimum acts as a wedge-shaped potential well, the frequency of the localized, exchange-dominated SWs can be calculated from:

$$f_n = (\gamma \frac{2A}{M_S}(\frac{n\pi}{m})^2)^{\frac{1}{3}} + 15.25 \text{ GHz}, \tag{2.1}$$

in which n is an integer, A is the exchange stiffness, m is the wedge slope (40 nm/GHz) of the potential well, and 15.25 GHz is the frequency at the bottom of the potential well. For n=1, Equation 2.1 yields $f_1 \approx$17 GHz, which is in good agreement with experiments and simulations. A detailed description of how the trapped mode frequency is calculated is given in Appendix A.

2.2.3 NC separation

Having robust synchronization in the vertical geometry makes it easier to increase the cc separation of the NCs. Figure 2.5(a) shows experimental measurements of two NCs with varying cc separations. Robust synchronization can be seen for separations of up to 1000 nm. When the NCs are 1300 nm apart, synchronized and unsynchronized states are observed in the samples; for cc =1400 nm, two peaks could be seen in all the measured devices, indicating that they are not synchronized. The loss of synchronization at such separations is consistent with the experimental results on SW propagation lengths in permalloy [32].

2.2.4 Synchronization of 5 NCSTOs

The vertical geometry not only provides robust synchronization over large separations, but also paves the way for synchronizing more than two NCs. Figure 2.5(b)–(d) demonstrates the experimental results for 3, 4, and 5 NCs; robust synchronization can be seen in all cases. The average integrated power, P_{ave}, and linewidth, Δf_{ave}, of the devices is [$P_{Ave,3-NC}$=3.3 pW, $\Delta f_{Ave,3-NC}$=27.1 MHz], [$P_{Ave,4-NC}$=5.3 pW, $\Delta f_{Ave,4-NC}$=14.0 MHz] and [$P_{Ave,5-NC}$=8.5 pW, $\Delta f_{Ave,5-NC}$=11.2 MHz], respectively. The increase (decrease) in power (linewidth) can be clearly seen as the number of devices increase. The synchronization in the 5-NC device can be manipulated by changing the in-plane field angle, $\Psi_{IP} = 30°$, as shown in Figure 2.5(c). By doing so, three modes can be observed in the same device. By analyzing the integrated power and linewidth of the modes shown in Figure 2.4(d), it can be concluded that four of the NCs are pairwise synchronized and that one is not locked at all.

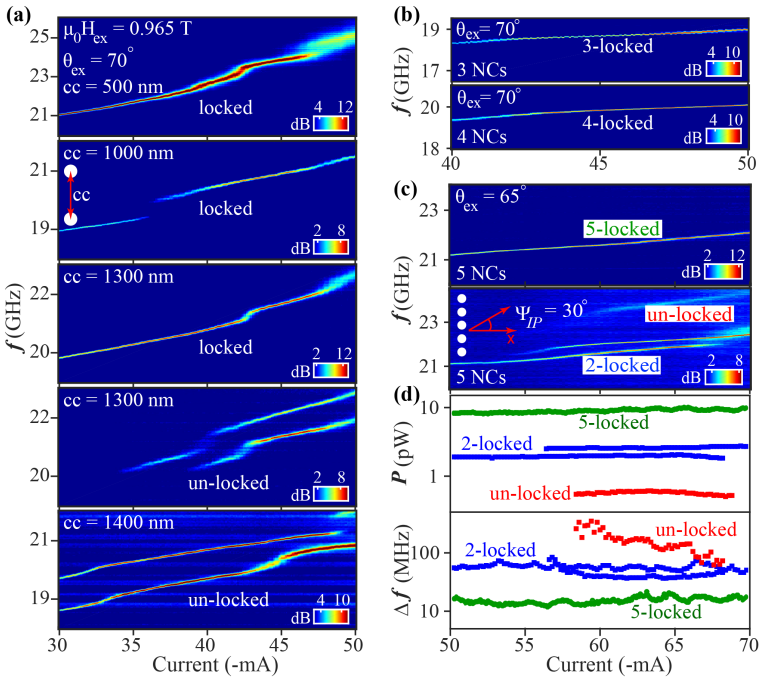

Figure 2.5: (a) All measured devices with two NCs of 100 nm nominal diameter show synchronization up to cc=1000nm. For cc=1300 nm, some devices show synchronization, and some do not. For larger separations, synchronization was not observed. (b) Robust synchronization of 3 and 4 NCs, respectively. (c) Synchronization of a 5-NC device over the entire current range. Synchronization can be broken by tilting the in-plane angle, Ψ_{IP} by 30°. (d) Comparing the integrated power and linewidth of the 5-NC device shown in part (c) for the synchronized and unsynchronized states, it can be concluded that there are two pairs of synchronized NCs and a single unsynchronized NC.

2.3 NCSTO Synchronization Challenges

The NCs in the investigated devices are connected in parallel with each other, and so as the number of the NCs increases, the current needed to drive them increases too. Increasing the current density could give rise to problems such as Joule heating. Initially, to investigate the effect of Joule heating on NCSTOs, the frequency response of a 2-NC device as a function of θ_{ex} was recorded, and is shown in Figure 2.6(a). As can be seen, the NCs are synchronized for $\theta_{ex} > 60°$. In the next step, I_{dc} was swept from -30 to -50 mA at a fixed $\theta_{ex} = 80°$ for ten consecutive times, and the change in the resistance of the devices was probed. Finally, the first measurement conducted on the sample was repeated, as shown in Figure 2.6(b). However, two modes can be detected for the same range of θ_{ex}, indicating that the NCs are no longer synchronized. The inset in Figure 2.6(b) shows a parabolic increase in the resistance of the

devices. Furthermore, the resistance of the devices increases monotonically after each successive measurement. It has been shown that, for the range of current densities that our devices are subjected to, the local temperature in the vicinity of the NC can reach as high as 170 K above the ambient temperature [141]. This increase in temperature could enhance the diffusion of Cu from the spacer and cap layers into the permalloy free layer and therefore increase its Gilbert damping.

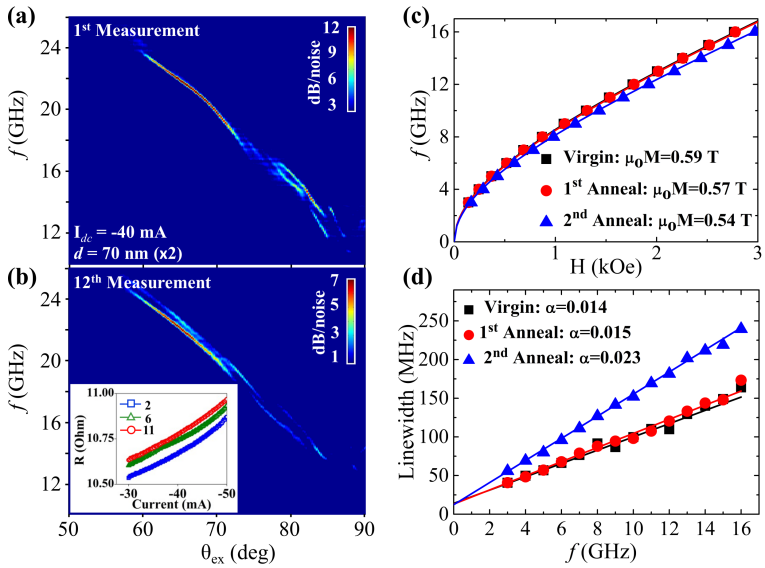

Figure 2.6: Experimental frequency spectra as a function of θ_{ex} from two NCSTOs with a nominal diameter of 70 nm and a cc spacing of 140 nm (a) after the first measurement, (b) after the twelfth measurement. The inset in (b) depicts the change in resistance during consecutive current sweep measurements. (c) Dependence of the FMR frequency on the external field; The solid lines are fits to the Kittel equation. (d) Dependence of the linewidth of the FMR response on the frequency; The lines are fit to Eq. 2.2, from which α and ΔH_0 can be extracted.

To investigate the effect of temperature on the damping characteristics of NiFe, FMR measurement was performed on three blank Cu(8 nm)/NiFe(4.5 nm)/Cu(3 nm)/Pd(3 nm) films. The first sample was used as a reference (virgin), the second was subjected to the same annealing process that the actual devices are subjected to during the fabrication process, and the third sample was subjected to 200° C in vacuum for 12 hours to mimic the conditions the sample experience during the measurement [141]. Figure 2.6(c) shows the saturation magnetization M_s, extracted from the Kittel equation, of the three blank films. As can be seen, M_s is lower in both of the annealed samples, which is consistent with the diffusion of Cu into NiFe. The Gilbert damping α can be calculated by probing the frequency dependence of FWHM [142]:

$$\Delta H = \frac{4\pi\alpha}{\gamma} f + \Delta H_0, \tag{2.2}$$

where ΔH_0 is the inhomogeneous broadening and is usually due to the intrinsic properties of the sample. As can be seen in Figure 2.6(d), all of the samples had the same ΔH_0. However, although the virgin and the first annealed sample have about the same damping, $\alpha = 0.014$, and 0.015, the second annealed sample has a significantly higher damping of 0.023. This higher value could hinder SW propagation, which is the main mechanism for the synchronization of NCSTOs. Furthermore, electromigration induced by high current densities [143] can cause irreversible structural damages and enhance the diffusion of Cu into NiFe.

3

Spin Hall Nano-oscillators (SHNOs)

The discovery of the SHE [90] has paved the way for many new applications [144–146]. Through asymmetric electron scattering in metals with high spin-orbit coupling, SHE can convert an unpolarized charge current into a transverse pure spin current. In this way, SHE could have many potential applications in STT-based microwave generation [147], since the pure spin current can exert a significant amount of STT on the adjacent ferromagnetic material [92, 148]. Above a certain threshold, SHE-induced STT could compensate for the natural damping of the medium and sustain auto-oscillation in a class of devices called SHNOs [12, 13, 17, 18, 149–151]. This new class of device has some advantages over NCSTOs, such as easier fabrication and direct optical access to the magnetodynamically active region.

3.1 Ultrasmall Nanoconstriction

The SHNOs studied in this thesis consist of a $Ni_{80}Fe_{20}$ 5 nm/Pt 6 nm bilayer. The IBE process at a tilted angle, in this case, 25°, reduced the lateral dimensions up to 30 nm. The devices with a nominal diameter of 50 nm thus had an actual width of 20 nm, as shown in Figure 3.1(b). AMR measurements were performed with a rotatable projected field magnet providing an in-plane (IP) and constant field of 90 mT. It should be noted that the IP field angle $\varphi = 0°$ refers to the condition where the magnetic field is perpendicular to the current flow direction, as shown in Figure 3.1(a). The AMR measurement results shown in Figure 3.1(c) give an overall value of 0.17 %, which is in good agreement with reported AMR values for extended films of Py/Pt [13]. The best fit with the AMR data is obtained by assuming that the external field, H, coherently rotates the magnetization on the basis of a Stoner–Wohlfarth model. The IP internal angle can thus be obtained from:

$$sin(\phi - \varphi_{int}) = \frac{H_k}{2H} sin(2\varphi_{int}), \tag{3.1}$$

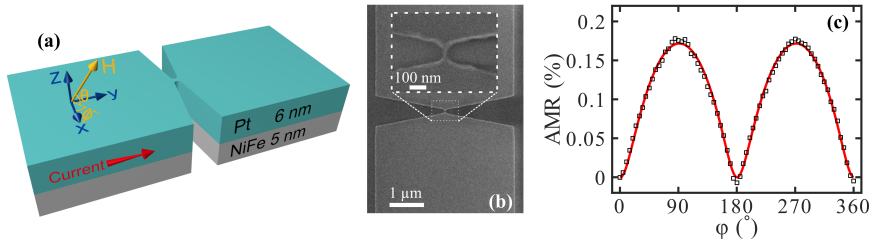

Figure 3.1: (a) Schematic of a nanoconstriction bilayer SHNO. φ shows the IP direction of the external field, H, and θ shows the out-of-plane angle. (b) SEM images of an SHNOs with an actual width of 20 nm. (c) AMR measurement showing a significant uniaxial anisotropy along the current flow direction, $\varphi = 90°$.

The best fit is obtained considering a significant uniaxial anisotropy of $\mu_0 H_k$= 41 mT along the y-axis, which has a considerable contribution from the shape anisotropy induced by the constriction along the current flow. Since the microwave response detection of the samples relies on the change in resistance, the local resistance minimum ($\varphi = 0°$) must be avoided; instead, an IP angle with a large $dR/d\varphi$ should be chosen. In all the following measurements, φ is thus taken as 24°.

The color plot in Figure 3.2(a) shows the spectral density of a 20 nm SHNO when μ_0H = 0.7 T and the out-of-plane (OOP) angle $\theta = 60°$. It is clear that the threshold current for auto-oscillations is $I_{th} = 0.54$ mA. The oscillation frequency increases and finally levels off at a maximum value of about 16.25 GHz. Even the highest oscillation frequency is still below the calculated FMR frequency of the extended film, 18.4 GHz, indicating that the excited mode is spatially localized. Figure 3.2(b) shows the frequency, power, and linewidth of the auto-oscillations at different OOP angles. As can be seen, the frequency increases when the OOP angle is tilted more towards the IP direction, which is consistent with the FMR frequency of obliquely magnetized films. The power (linewidth) increases (decreases) exponentially with a clear dependence on field angle. However, the situation is a little different for $\theta = 40°$, which might be due to a change in the nature of the mode from a localized mode at high OOP angles to the FMR-like mode observed for smaller IP applied fields [18]. Furthermore, The threshold current also depends on the applied field angle and is at its minimum for $\theta = 60°$, as shown in the inset of Figure 3.2(a). Micromagnetic simulations were conducted to understand the nature of the auto-oscillation. The current distribution and the current-induced Oersted field were simulated using COMSOL Multiphysics software, and the results obtained were later used as inputs in MUMAX3. The effective magnetization and Gilbert damping used in the simulations are measured to be μ_0M = 0.7 T and $\alpha = 0.02$, respectively [152, 153]. It is also shown that taking the spin Hall angle to be 0.07 yields remarkable agreement between experiments and simulations [154].

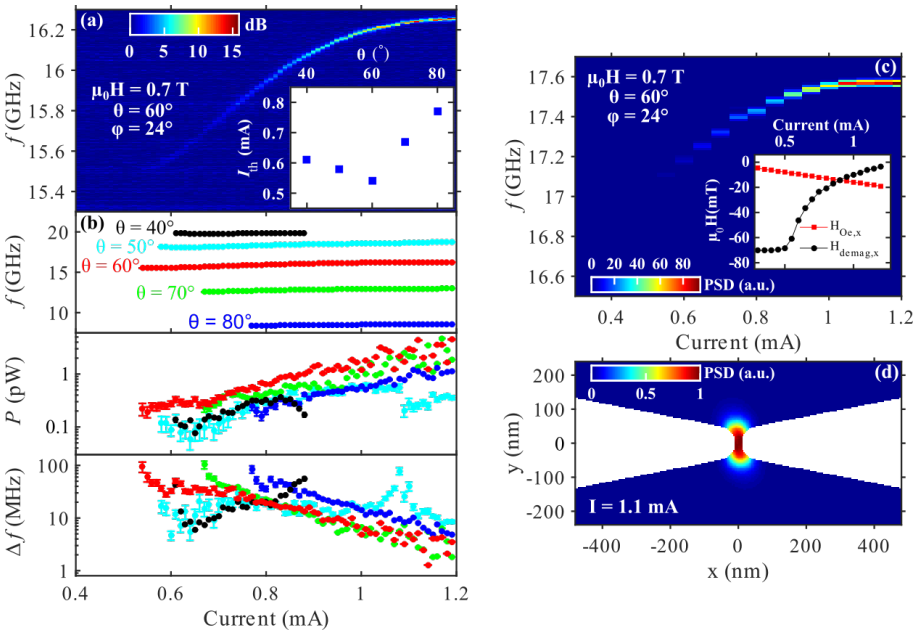

Figure 3.2: (a) Power spectral density on a logarithmic scale as a function of applied current. (b) Frequency, power, and linewidth of the auto-oscillation for several OOP angles as a function of applied current. (c) Micromagnetic simulation of power spectral density as a function of applied current. The inset shows the x-component of the current-induced Oersted field (red squares) and demagnetizing field (black dots) at the center of the constriction. (d) Simulated mode energy distribution at 1.1 mA, showing that the mode is localized in the center of the constriction.

Although analytical calculations predict red-shifting with current for localized modes [34], the experiments and simulations shown in Figure 3.2 clearly suggest otherwise. The simulated power spectral density in Figure 3.2(c) shows blue-shifting as the current is increased, corroborating the experimental results (Fig. 3.2(a)). To understand this, all the contributions to the magnetic field need to be considered: (1) the current-induced Oersted field and (2) the demagnetizing field due to the finite lateral size of the nanoconstriction. The IP component of the Oersted field is opposite to the external field; therefore, as the current is increased, the effective magnetic field and its OOP angle decreases, causing a negative current tunability. As with the Oersted field, the direction of the demagnetizing field is also opposite to the external field. However, when the auto-oscillation begins, the static magnetization is reduced due to the precessional motion of the magnetization, which in turn reduces the demagnetizing field within the constriction. As the auto-oscillation amplitude is increased by increasing the current, the average demagnetizing field is reduced, giving rise to a positive current tunability. The inset to Figure 3.2(c) shows the x-component of the simulated Oersted field and demagnetizing field at

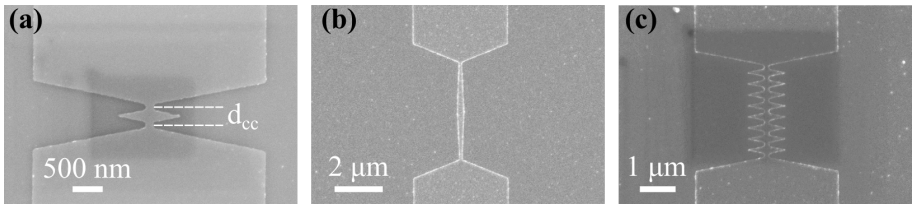

Figure 3.3: (a) SEM image of an SHNO with two 150 nm constrictions and a separation of d_{cc} =300 nm. (b) SEM image of a device with two 150 nm constrictions connected by a bridge that opens up only about 5°. The constriction separation is $d_{cc} = 4\mu$m. (c) SEM image of a device with nine 150 nm constrictions, each pair separated by 300 nm.

the center of the constriction, which clearly justifies the observed frequency dependence of the auto-oscillations. Figure 3.2(d) presents the simulated distribution of the mode energy at 1.1 mA, which shows a localized mode at the center of the constriction, confirming the solitonic nature of the mode.

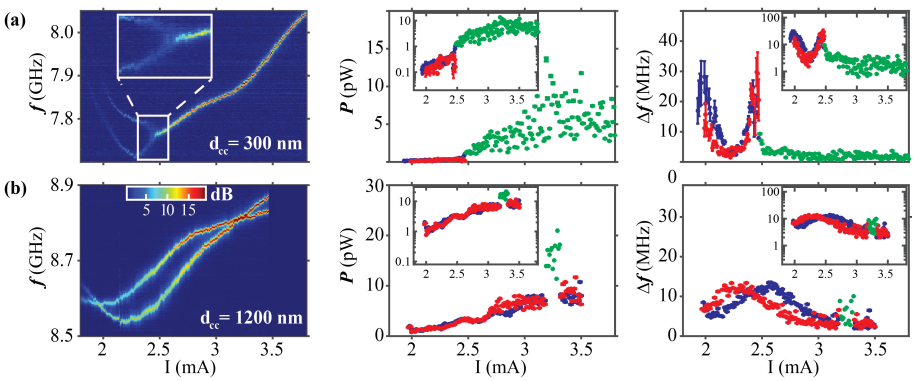

Figure 3.4: (a) SEM image of an SHNO with two 150 nm constrictions and a separation of d_{cc} =300 nm. (b) SEM image of a device with two 150 nm constrictions connected by a bridge that opens up only about 5°. The constriction separation is $d_{cc} = 4\mu$m. (c) SEM image of a device with nine 150 nm constrictions, each pair separated by 300 nm.

3.2 Mutual Synchronization of SHNOs

Mutual synchronization is attempted to improve the output power of the SHNOs. The high nonlinearity of STNOs generally, and of SHNOs specifically, can promote SW-mediated mutual synchronization [62–64, 112]. It was mentioned in Chapter 2 that propagating SW modes are required for synchronization to occur. However, it has been shown in the previous section that the excited mode in nanoconstrictions is localized even for OOP field

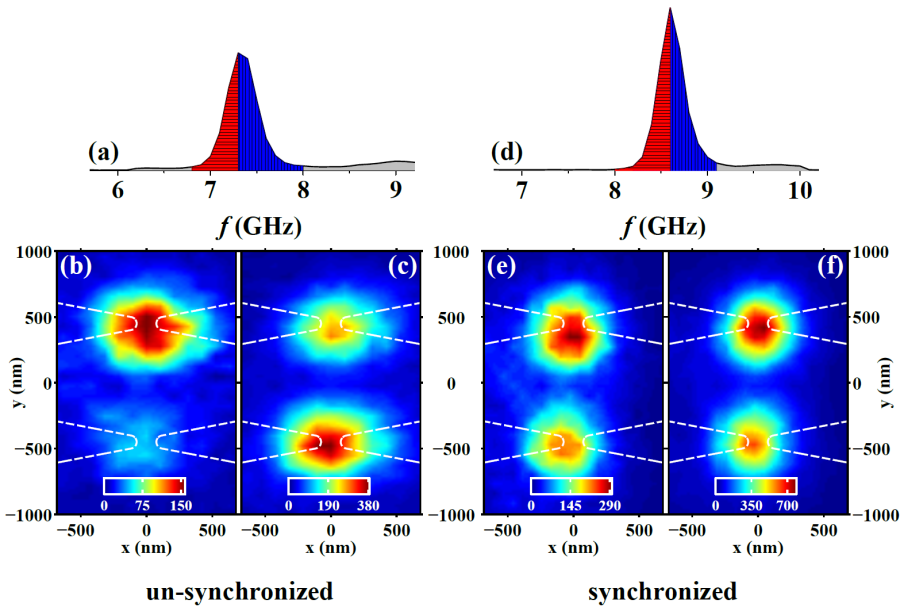

Figure 3.5: (a) μ-BLS frequency spectra for an unsynchronized state. (b) and (c) Spatial maps of the oscillation amplitude for the lower and upper frequency regions, respectively. Only one constriction is energized at a time, indicating that the constrictions are not synchronized. (d) μ-BLS frequency spectra for a synchronized state. (e) and (f) Spatial maps of the oscillation amplitude for the lower and upper frequency regions, respectively. Both constrictions are energized over the whole frequency region, indicating they are synchronized

angles. To reduce the localization and achieve a positive nonlinearity [33, 101, 132], the OOP field angle was chosen to be $\theta = 80°$, whereas the IP angle was kept at $\varphi = 24°$. A SEM image of a typical SHNO with two 150 nm constrictions and a separation of 300 nm is shown in Figure 3.3(a). Figure 3.4 (a)–(b) summarizes the synchronization of devices with two nanoconstrictions having a nominal width of 120 nm and a separation d_{cc} of 300 nm and 1.2 μm, respectively. At low current, each device shows two individual, noninteracting signals. When the current is increased, the weak signals merge into a much stronger signal at 300 nm separation. For a separation of 1.2 μm, regions of mutual synchronization can be observed when the current is increased. With this geometry, synchronization could not be seen for separations larger than 1.2 μm. Here again, synchronization is characterized by an increase in power and a reduction in linewidth compared with the unsynchronized states [101].

As mentioned earlier, the unique device geometry of SHNOs allows optical access to the magnetodynamically active area. As a result, synchronization of SHNOs can be optically observed by μ-BLS measurement, as shown in Figure 3.5, from two constrictions with $d_{cc} = 900$ nm. Since the frequency resolution of the BLS is limited, only one peak can be detected for both the

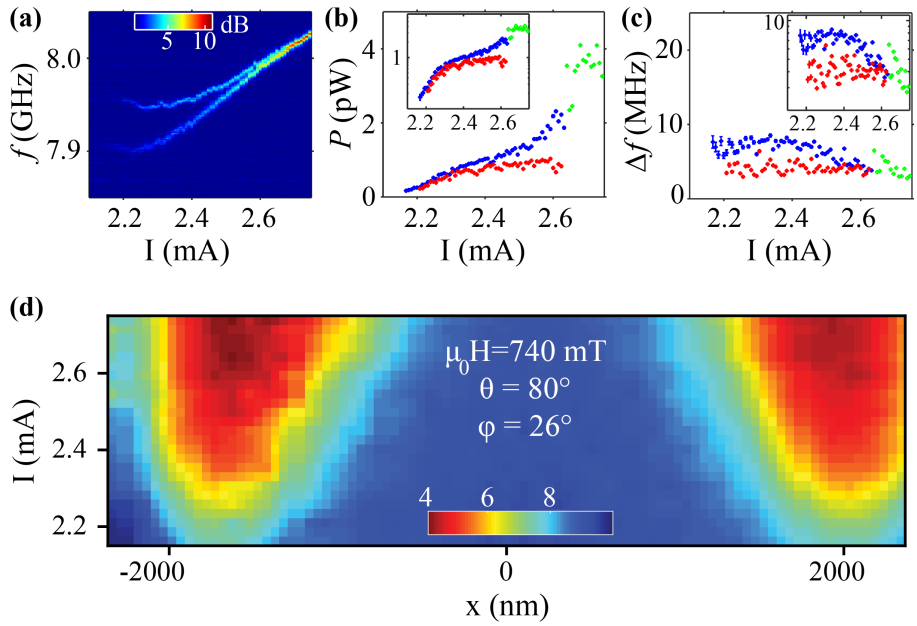

Figure 3.6: (a),(b), and (c) are the power spectral density, integrated power, and linewidth of of two 140-nm nanoconstrictions as a function of current in an applied field of 0.745 mT, with $\varphi = 26°$ and $\theta = 80°$. (d) μ-BLS (logarithmic scale) along the center of the device with increasing current.

synchronized (Figure 3.5(a)) and unsynchronized cases (Figure 3.5(d)). To distinguish between the two cases, the BLS map can be divided into two parts, each covering a different frequency range. In the unsynchronized case, the BLS map in the low-frequency range (red in Figure 3.5(a)) shows that only the upper constriction is energized; in the high-frequency range (colored blue), the lower constriction is energized. However, when the constrictions are synchronized, both are energized over the whole frequency range of the BLS maps, as shown in Figure 3.5(d)–(f).

3.2.1 Long-Range Synchronization

As previously discussed, synchronization could not be achieved for separations larger than 1.2 μm. This is most likely due to the damping in the bridge connecting the constrictions. To overcome this, the bridge is designed so that although the local current concentration is below the threshold of auto-oscillations, it is sufficiently large to enlarge the subthreshold precession between the constrictions. To that end, a device was designed consisting of two 140 nm constrictions separated by 4 μm, with a bridge that only opens up 5°, as shown in Figure 3.3(c). The electrical microwave signal of the device is shown in Figure 3.6(a). Two signals can be detected for currents less than 2.6 mA. However, the signals merge as the current is increased, with an increase

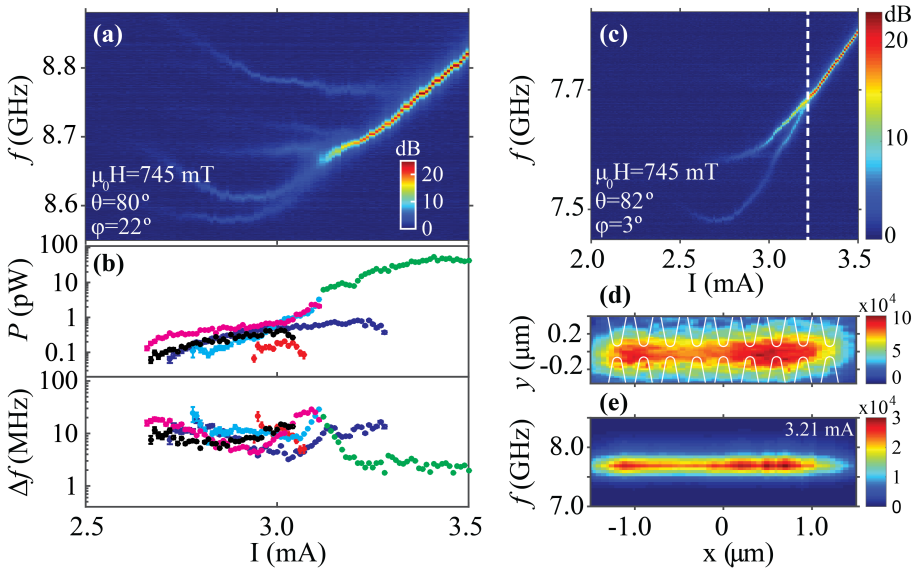

Figure 3.7: (a) Power spectral density as a function of current of an SHNO with nine 120-nm constrictions separated by 300 nm in an applied field of 745 mT along $\varphi = 22°$ and $\theta = 80°$. (b) Output power and linewidth of the individual peaks and the synchronized state. (c) Power spectral density as a function of current of an SHNO with nine 120-nm constrictions separated by 300 nm in an applied field of 745 mT along $\varphi = 3°$ and $\theta = 82°$. (d) μ-BLS spatial map of the synchronized SHNO. (e) μ-BLS frequency map of the synchronized SHNO along y = 0.

in power and a decrease in the linewidth (Figure 3.6(b)–(c))—the signatures of synchronization. The long-range nature of the synchronization appears to be due to the reduced damping in the connecting bridge and the expansion of the auto-oscillation regions with the increase of current, as shown in Figure 3.6(d), which is the spatial profile of the auto-oscillations as a function of applied current as observed by μ-BLS.

3.2.2 Synchronization of Multiple Nanoconstrictions

Having achieved synchronization of two nanoconstrictions with large separations, constrictions with as many as eleven constrictions and a fixed separation of 300 nm were fabricated to see how many oscillators could be mutually synchronized. The maximum number of mutually synchronized constrictions observed was nine, as shown in Figure 3.7(a). At low currents, each constriction generates a specific microwave signal. As the current is increased, partial synchronization is achieved, and then, at about 3.29 mA, a global synchronization is observed. The maximum power of the synchronized device (Figure 3.7(b)) is 54 pW—much higher than the sum of the power of individual constrictions

($\approx$ 1 pW for each individual nanoconstriction). μ-BLS was used to verify and map the synchronization of nine constrictions, as shown in Figure 3.7(c). When synchronized, the μ-BLS maps (Figure 3.7(d)–(e)) show that all the nine constrictions have the same frequency and similar amplitudes. The reason the auto-oscillation region is seen as continuous is due to the diffraction limitation (360 nm) of the μ-BLS.

4

Hybrid Magnetic Tunnel Junctions

In the previous two chapters, synchronization was presented as a method to increase the output power of STOs. When high power is needed, even synchronized networks of NCSTOs and SHNOs lag behind STOs based on MTJs. It has been shown that MgO-based MTJs can deliver high powers on the order of μWs [75, 78, 79]. However, MTJs based on nanopillar structure suffer from larger linewidths than NCSTOs [72, 102–104]. In the following, the basic characterization of a tailored MTJ device (a so-called hybrid MTJ) is presented, and it is shown that such devices have great potential regarding applicability when low linewidth and high output powers are necessary [155, 156]. The MTJ stack used in this study has been deposited at the International Iberian Nanotechnology Laboratory. The complete layer sequence is: Ta(3)/CuN(30)/Ta(5)/PtMn(20)/$CoFe_{30}$(2)/Ru(0.85)/
$CoFe_{40}B_{20}$(2)/$CoFe_{30}$(0.5)/MgO/$CoFe_{30}$(0.5)/
$CoFe_{40}B_{20}$(1.5)/Ta(3)/Ru(7). Hybrid NCMTJ devices (Figure 1.8) were fabricated from this stack and microwave measurement was performed to analyze their magnetodynamical behavior. The upper CoFeB/CoFe bilayer acts as the free layer (FL), which is separated from another bilayer of CoFeB/CoFe, the reference layer (RL), by a MgO barrier. The resistance-area product of the MgO barrier is 1.5 Ω μm^2. The pinned layer (PL) is formed of CoFe with an antiferromagnetic PtMn pinned layer (PL) underneath. A schematic of the final device and the stack sequence is shown in Figure 4.1(a).

4.1 Basic Characterization

The magnetization hysteresis loop of a blank film and the MR measurements performed on a device are shown in Figure 4.1(b) and (c), respectively. The magnetic state of some important points is demonstrated in Figure 4.1(b). In each state, PL, RL, and FL represent the pinned layer, reference layer, and free layer, respectively. The thick black line between the FL and RL layers stands for the MgO barrier. The point corresponding to each state in Figure 4.1(b) is shown in the MR hysteresis (Figure 4.1(c)). MR is primarily determined by

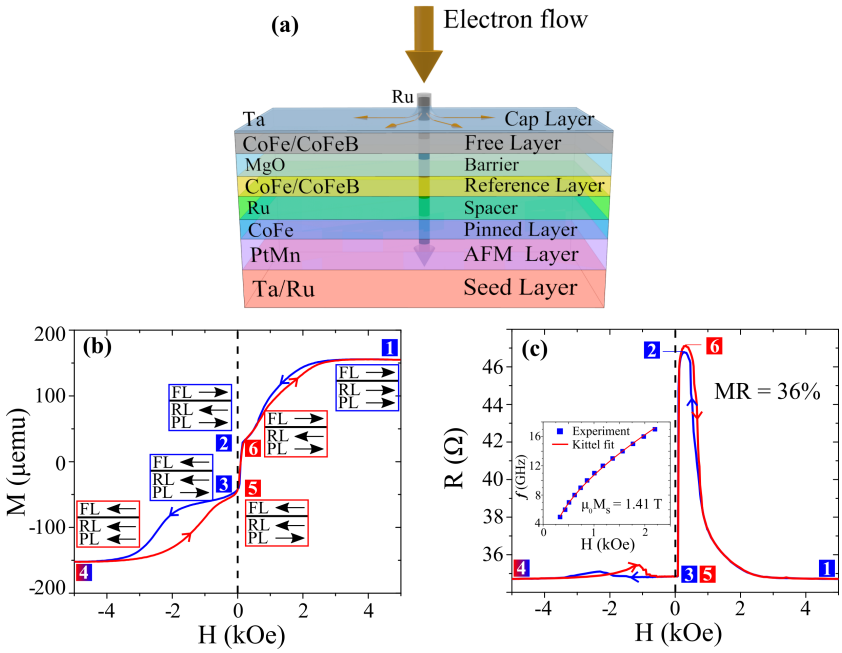

Figure 4.1: (a) Schematic of a hybrid MTJ device with arrows showing the current flow in the cap and through the layers. (b) MR results along the EA direction of the MTJ film. The blue and red curves show the In all of the cases, the solid red line shows the ascending branch, and the solid blue line shows the descending branch of the hysteresis loop and MR data. The inset in (b) is the frequency of the uniform FMR mode as a function of the field. The red solid line is the fit made by the equation in the inset of the figure.

the relative orientation of FL and RL with respect to each other. As expected, the maximum of MR is obtained when RL and FL point opposite to each other (states 2 and 6). The maximum MR in our hybrid devices is about 36%, far greater than the typical $\approx 1\%$ for all-metallic GMR-based NCSTOs [76]. This significant difference in MR translates into the output power of the devices, as will be shown later on. The inset of Figure 4.1(c) shows the broadband FMR measurements (blue squares). The red line shows the Kittel equation, which fits the FMR data well. From the fit, the gyromagnetic ratio and saturation magnetization can be determined to be $\gamma/2\pi = 29.7$ GHz/T and $\mu_0 M_s = 1.41$ T, respectively.

4.2 Magnetization Dynamics

In the first step, the microwave response of a hybrid MTJ with a nominal diameter of 150 nm was recorded as a function of the external field angle θ_{ex} at a fixed bias current $I_{dc} = -5$ mA and an external field $\mu_0 H = 9.65$ kOe. The

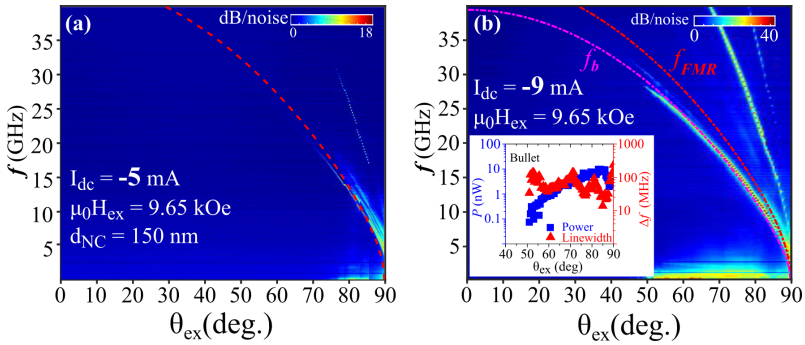

Figure 4.2: (a) Microwave response of a hybrid MTJ with a nominal diameter of 150 nm as a function of applied field angle at a fixed field of μ_0H = 9.65 kOe and $I_{dc} = -5$ mA. A broad FMR-like mode together with a sharp mode having a frequency lower than FMR (a bullet) is observed. By increasing the current to (b) -9 mA, the bullet can be better distinguished. The red and pink dashed lines are the calculated FMR and bullet frequencies. The inset in (b) shows the power and linewidth of the bullet for 40° $\leq\theta_{ex}\leq$90° with $\theta_{ex} = 90°$

result is shown in Figure 4.2(a), with the red dashed line representing the FMR frequency calculated by solving the magnetostatic boundary conditions (Eq. 1.8). As can be seen, at $\theta_{ex} > 75°$, a broad signal is observed which resembles a thermal FMR mode [35, 157]. In addition to this, a second sharper mode with a lower frequency than FMR is observed, together with its second harmonic. Furthermore, a broad low-frequency response, f <3 GHz, can be seen, which is usually associated with mode hopping [36]. The nature of the auto-oscillations is revealed by calculating the angular dependence of the nonlinear frequency shift from [34]:

$$N = \frac{\omega_H \omega_M}{\omega_{fmr}} \left(\frac{3\omega_H^2 sin\theta_{int}^2}{\omega_{fmr}^2} - 1\right), \tag{4.1}$$

where ω_{fmr} is the FMR angular frequency, $\omega_H = \gamma H_{int}$, $\omega_M = 4\pi\gamma M_s$, and finally H_{int} and θ_{int} are the internal magnetic field magnitude and out-of-plane angle, respectively. γ is the gyromagnetic ratio, and M_s is the saturation magnetization of the composite CoFe/CoFeB free layer. Furthermore, H_{int} and θ_{int} are extracted by solving the magnetostatic boundary conditions, Equation 1.8. Calculations show that N is negative for the entire range of 0° $\leq\theta_{ex}\leq$90°, with $\theta_{ex} = 90°$ being perpendicular to the sample surface. This means that the only stable mode within this range is a solitonic bullet mode [33, 34, 104]. By increasing the current to $I_{dc} = -9$ mA, the bullet mode reveals itself more clearly, as can be seen in Fig. 4.2(b). The frequency of the bullet mode can be calculated from [33]:

$$\omega_b = \omega_{fmr} + NB_0^2, \tag{4.2}$$

where ω_b is the bullet angular frequency and B_0 is the characteristic spin wave

amplitude. The calculated ω_b, shown by the pink dashed line in Figure 4.2(b), quantitatively describes the frequency and angular dependence of mode 2 by setting B_0=0.46 [33], providing further evidence that this mode is, in fact, a solitonic bullet. The inset to Figure 4.2(b) shows the power and linewidth of the bullet as a function of θ_{ex}. The power of the bullet increases with θ_{ex} while the linewidth remains almost constant. This behavior is consistent with the previously reported angular dependence of the power and linewidth of bullets [104].

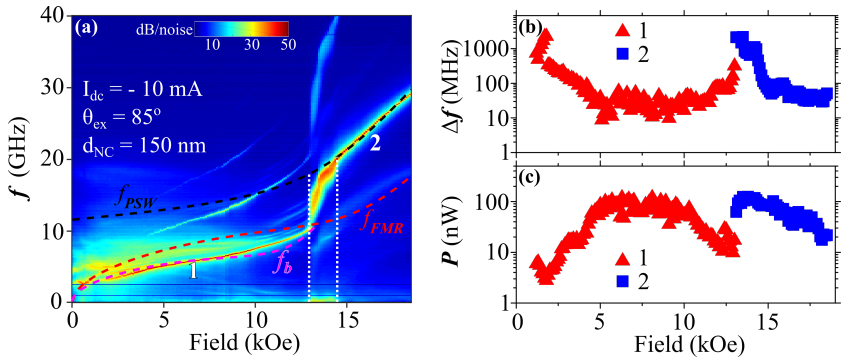

Figure 4.3: (a) Microwave response of a hybrid MTJ with a nominal diameter of 150 nm as a function of applied magnetic field at $I_{dc} = -10$ mA and $\theta_{ex} = 85°$. The pink, red, and black dashed lines represent the calculated bullet, FMR, and propagating SW frequency, respectively. (b) and (c) show the linewidth and power of mode 1 (bullet) and mode 2 (propagating mode).

The microwave response of the same device as a function of the external field is shown in Figure 4.3(a). As can be seen, for applied fields below about 13.5 kOe, a sharp high-power mode, mode 1, exists with a frequency lower than FMR, represented by a red dashed line. The bullet frequency, calculated according to Equations 4.1 and 4.2 and represented by the pink dashed line, shows good agreement with mode 1, suggesting that this mode is a bullet. However, above 13.5 kOe, mode 2 has a frequency well above FMR. This clearly suggests that mode 2 is fundamentally different from mode 1, in the sense that it must be propagating with a wave-vector $k \approx 1.2/R_c$ [30, 33]. The frequency of a propagating SW (PSW) mode can be obtained from the Slonczewski equation [30]:

$$f_{PSW} = 2\pi\gamma(H_{int} + \frac{2A_{ex}k^2}{M_s}), \tag{4.3}$$

in which the exchange stiffness is $A_{ex} = 28 \times 10^{-12}$ J/m [158]. The calculated PSW frequency is shown with a black dashed line in Figure 4.3(a) and shows perfect agreement with experimental results. Having a PSW could have far-reaching consequences, such as allowing the synchronization of multiple hybrid MTJs. In the transition region between mode 1 and 2, enclosed by the white dotted line in Figure 4.3(a), a broad mode exists together with a very low

(<1 GHz) frequency response, which is a signature of mode hopping between the bullet and the propagating mode [22, 36]. The linewidth and integrated power of both mode 1 and 2 are shown in Figure 4.3(b) and (c), respectively. As can be seen, the output power of a single hybrid MTJ is about 100 times greater than that of all metallic GMR-based NCSTOs, while their linewidths are comparable.

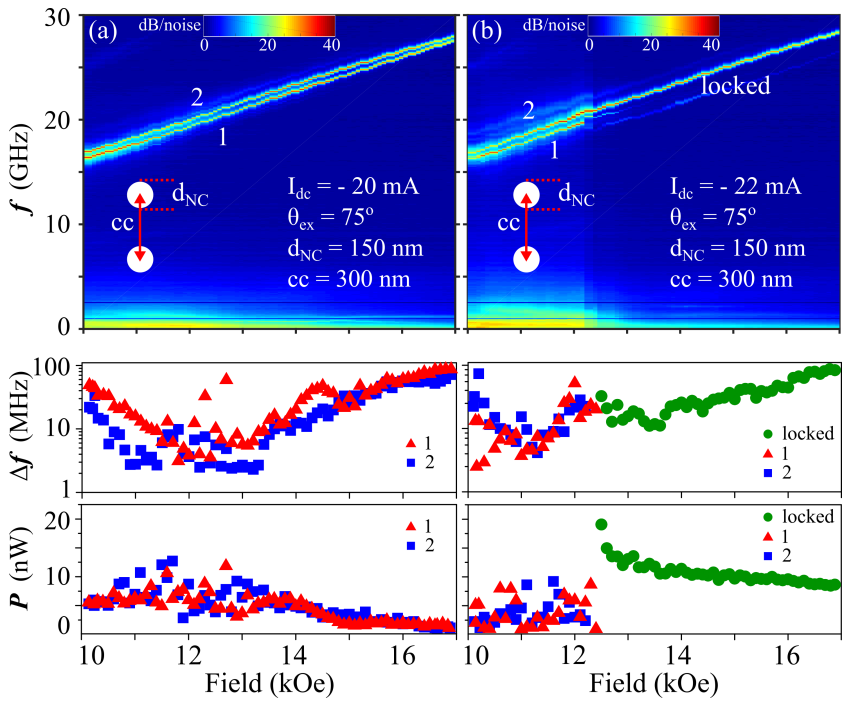

Figure 4.4: Microwave response of a double-NC hybrid MTJ. Each NC has a diameter of 150 nm and a cc spacing of 300 nm at (a) -20 mA: Two modes corresponding to each of the NCs can be seen. The average power and linewidth of each NC is about 5 nW and 30 MHz, respectively. (b) -22 mA: two modes can be seen for magnetic fields up to 12.3 kOe, but only one strong mode can be observed for magnetic fields from 12.3 kOe to 17 kOe, which suggests modes 1 and 2 are synchronized. The average power of the synchronized mode is greater than that of each of the single modes.

As mentioned earlier, the implementation of PSWs in hybrid MTJs paves the way for the synchronization of multiple NCs. To that end, we fabricated hybrid MTJs with two NCs having a nominal diameter of 150 nm and a centre-to-centre spacing of 300 nm. The results of field sweeps from 10 kOe to 17 kOe at two different currents are shown in Figure 4.4. At -20 mA, two modes (modes 1 and 2) can be observed, each having an average power of about 5 nW and and average linewidth of about 30 MHz. Increasing the current to -22 mA, two modes can at first be detected, but only one mode remains when the

magnetic field rises above 12.3 kOe. Analyzing the power of these modes shows that the power of the "locked" mode is higher than modes 1 and 2, suggesting they are synchronized. Furthermore, the low-frequency signal, a signature of mode hopping, almost disappears after the modes are locked. While these results are preliminary, they clearly show a potential for synchronizing multiple hybrid NC-MTJs and could increase the power and mode uniformity of these devices even further, making them suitable for applications [159–161].

5

Conclusions and outlook

In this thesis, different classes of spin-torque oscillators were fabricated and studied. The main theme of this thesis was to achieve synchronization in these devices and to therefore improve their output power and mode uniformity, making them more suitable for applications. In the following, a summary of the results is presented together with some suggestion for future study.

In terms of fabrication, apart from fabricating devices with multiple NCs in NC-STOs, or multiple constrictions in SHNOs, a new class of devices was fabricated based on MTJs. The new devices combine the advantages of NC-based STOs and NP-based MTJs into a new hybrid device. Being able to fabricate MTJs with an extended free layer opens up previously unavailable opportunities, like the synchronization of multiple hybrid NC-MTJs and the realization of new magnetization dynamics that were previously observed only in all-metallic devices.

In Chapter 2, the synchronization of NC-STOs was discussed and the critical role of the Oersted field and its effect on the SW propagation pattern was explored. It was shown that the Oersted field not only localizes spin waves, but also causes their asymmetric propagation, with far-reaching consequences. Synchronization in such cases is no longer mutual, but is "*driven*" by the NC from which the SWs were emitted. Furthermore, by simply daisy-chaining any number of NC-STOs, SW propagation length can be extended to much larger distances, allowing them to transfer information and form a kind of SW repeater. One can take advantage of SW directionality and control the synchronization state by changing the direction of the in-plane applied field, steering the SW beam in the desired direction. This concept is schematically shown in Figure 5.1, in which discs of the same color represent synchronized NCs and the green arrows show the SW propagation direction corresponding to different in-plane applied fields.

Robust synchronization of multiple nanoconstriction devices both over large distances and large numbers was demonstrated in Chapter 3. Simple fabrication, direct optical access to these devices, and robust synchronization over large distances and numbers all open up intriguing possibilities in both analog and digital spin-wave computing [162–164]. More complex structures, such as spin-wave majority gates, can be envisioned [165]. Although the microwave power is still orders of magnitude lower than that of MTJ-based STOs, three-terminal

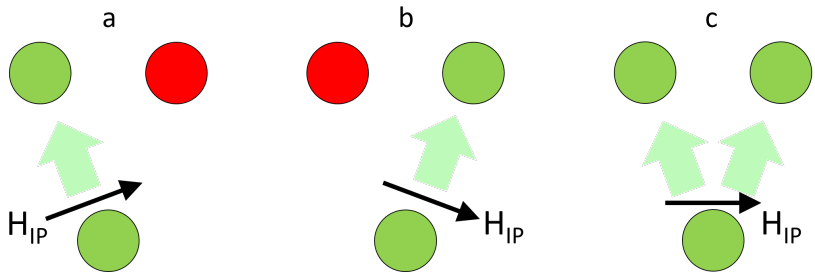

Figure 5.1: Schematic representation of synchronization state in a 2D array of NC-STOs. By controlling the in-plane component of the field, synchronization can be controlled between the bottommost and (a) upper-left, (b) upper-right, or (c) all three oscillators.

devices combining SHNOs and MTJ-based STOs are expected to perform even better. In such devices, synchronized SHNOs would generate SW power that will be converted to microwave power by MTJs fabricated on top of each oscillating region, providing yet another increase in power.

Chapter 4 focuses on a new class of MTJ-based STOs—namely, hybrid NCMTJs. Although operation of these devices has been demonstrated in both in-plane and out-of-place fields, very little is known about the nature of the excited SW modes. In this thesis, their magnetodynamical behavior is studied as a function of current, magnetic field magnitude, and magnetic field angle. Clear evidence of propagating SWs and of SW bullets has been seen and their field-dependent frequency has been fit with remarkable agreement. Having demonstrated the existence of propagating SWs, synchronization of such devices has been attempted and the preliminary results show promising results.

All the various classes of device studied in this thesis may act as building blocks of magnonics [166] and the emerging neuromorphic computing field. Neuromorphics is inspired by the biological functionality of the human brain and attempts to mimic it [167]. Neural networks can perform associative memory tasks through self-synchronization. Achieving and controlling synchronization in the nonlinear oscillators studied in this thesis, paves the way for mimicking such tasks, and may be even more scalable than biological neurons that work on much larger scales ($\simeq$1 μm).

Appendix

A

Allowed Frequencies in the Oersted-Field-Induced Potential Well

We have a potential wedge in frequency versus space, with the tilt given by a slope m in nm/GHz. Visually, it is easier to consider the slope $M = 1/m$ given in GHz/nm. The minimum of the potential well is the FMR frequency f_0. We want to know the n allowed frequencies inside the potential well.

Derivation

The n allowed frequencies in the potential well are given by

$$f_n - f_0 = \frac{nM\lambda}{2}, \tag{A.1}$$

where we simply write the equation of the tilted side of the wedge with respect to the FMR frequency. The "distance" of each allowed frequency is $\lambda/2$—i.e., half the wavelength, so that the wave begins and ends at zero.

On the other hand, exchange-mediated spin waves must obey the dispersion relation

$$f = f_0 + \gamma \frac{2A}{M_s} \left(\frac{2\pi}{\lambda}\right)^2, \tag{A.2}$$

where γ is the gyromagnetic ratio, A is the exchange stiffness, M_s the saturation magnetization, and we have taken $k = 2\pi/\lambda$. For simplicity, we will take $l = \gamma 2A/M_s$.

It is clear that f_n and f must be equal for f_n to be physically allowed, as we require in the problem formulation. It is also clear that f_0 is just a shift. So, setting $f = f_n$ and combining Equations (A.1) and (A.2)

$$\begin{aligned} \frac{nM\lambda}{2} &= l\left(\frac{2\pi}{\lambda}\right)^2 \quad \rightarrow \\ \left(\frac{\lambda}{2}\right)^3 &= \frac{l\pi^2}{nM} \end{aligned} \tag{A.3}$$

Replacing $\lambda/2$ in Equation (A.2)

$$\begin{aligned} f &= f_0 + l\pi^2 \left(\frac{nM}{l\pi^2}\right)^{2/3} \quad \rightarrow \\ f &= f_0 + \left(l(nM\pi)^2\right)^{1/3} \end{aligned} \tag{A.4}$$

Inserting $m = 1/M$ and $l = \gamma 2A/M_s$, we recover the equation as reported in Chapter 2 of this thesis.

Bibliography

[1] S. A. Wolf, D. D. Awschalom, R. A. Buhrman, J. M. Daughton, S. von Molnár, M. L. Roukes, A. Y. Chtchelkanova, and D. M. Treger, "*Spintronics: A Spin-Based Electronics Vision for the Future*", Science **294**, 1488–1495 (2001).

[2] A. Fert, "*Nobel Lecture: Origin, development, and future of spintronics*", Rev. Mod. Phys. **80**, 1517–1530 (2008).

[3] J. C. Slonczewski, "*Current-driven excitation of magnetic multilayers*", J. Magn. Magn. Mater. **159**, L1–L7 (1996).

[4] L. Berger, "*Emission of spin waves by a magnetic multilayer traversed by a current*", Phys. Rev. B **54**, 9353–9358 (1996).

[5] M. Tsoi, A. G. M. Jansen, J. Bass, W.-C. Chiang, M. Seck, V. Tsoi, and P. Wyder, "*Excitation of a Magnetic Multilayer by an Electric Current*", Phys. Rev. Lett. **80**, 4281–4284 (1998).

[6] E. B. Myers, D. C. Ralph, J. A. Katine, R. N. Louie, and R. A. Buhrman, "*Current-Induced Switching of Domains in Magnetic Multilayer Devices*", Science **285**, 867–870 (1999).

[7] S. I. Kiselev, J. C. Sankey, I. N. Krivorotov, N. C. Emley, R. J. Schoelkopf, R. A. Buhrman, and D. C. Ralph, "*Microwave oscillations of a nanomagnet driven by a spin-polarized current*", Nature **425**, 380–383 (2003).

[8] W. Rippard, M. Pufall, S. Kaka, S. Russek, and T. Silva, "*Direct-Current Induced Dynamics in* $Co_{90}Fe_{10}/Ni_{80}Fe_{20}$ *Point Contacts*", Phys. Rev. Lett. **92**, 027201 (2004).

[9] I. N. Krivorotov, N. C. Emley, J. C. Sankey, S. I. Kiselev, D. C. Ralph, and R. A. Buhrman, "*Time-Domain Measurements of Nanomagnet Dynamics Driven by Spin-Transfer Torques*", Science **307**, 228–231 (2005).

[10] T. J. Silva and W. H. Rippard, "*Developments in nano-oscillators based upon spin-transfer point-contact devices*", J. Magn. Magn. Mater. **320**, 1260–1271 (2008).

[11] J.-V. Kim, "*Chapter Four - Spin-Torque Oscillators*", in *Solid State Physics*, Vol. 63, edited by Robert E. Camley and Robert L. Stamps (Academic Press, 2012) Chap. 4, pp. 217–294.

[12] V. E. Demidov, S. Urazhdin, H. Ulrichs, V. Tiberkevich, A. Slavin, D. Baither, G. Schmitz, and S. O. Demokritov, "*Magnetic nano-oscillator driven by pure spin current*", Nature Mater. **11**, 1028–1031 (2012).

[13] R. H. Liu, W. L. Lim, and S. Urazhdin, "*Spectral Characteristics of the Microwave Emission by the Spin Hall Nano-Oscillator*", Phys. Rev. Lett. **110**, 147601 (2013).

[14] P. Dürrenfeld, F. Gerhard, S. M. Mohseni, M. Ranjbar, S. R. Sani, S. Chung, C. Gould, L. W. Molenkamp, and J. Åkermankerman, "*Low-current, narrow-linewidth microwave signal generation in NiMnSb based single-layer nanocontact spin-torque oscillators*", Appl. Phys. Lett. **109**, 222403 (2016).

[15] E. O. B. Parra, N. Bukin, M. Dupraz, G. Beutier, S. R. Sani, H. Popescu, S. A. Cavill, J. Åkerman, N. Jaouen, P. S. Keatley, R. J. Hicken, G. van der Laan, and F. Y. Ogrin, "*Holographic Magnetic Imaging of Single-Layer Nanocontact Spin-Transfer Oscillators*", IEEE Trans. Magn. **52**, 1–4 (2016).

[16] S. Sani, P. Dürrenfeld, S. Mohseni, S. Chung, and J. Åkerman, "*Microwave Signal Generation in Single-Layer Nano-Contact Spin Torque Oscillators*", IEEE Trans. Magn. **49**, 4331–4334 (2013).

[17] Z. Duan, A. Smith, L. Yang, B. Youngblood, J. Lindner, V. E. Demidov, S. O. Demokritov, and I. N. Krivorotov, "*Nanowire spin torque oscillator driven by spin orbit torques*", Nat. Commun. **5**, 5616 (2014).

[18] V. E. Demidov, S. Urazhdin, A. Zholud, A. V. Sadovnikov, and S. O. Demokritov, "*Nanoconstriction-based spin-Hall nano-oscillator*", Appl. Phys. Lett. **105**, 172410 (2014).

[19] S. Langenfeld, V. Tshitoyan, Z. Fang, A. Wells, T. A. Moore, and A. J. Ferguson, "*Exchange magnon induced resistance asymmetry in permalloy spin-Hall oscillators*", Appl. Phys. Lett. **108** (2016).

[20] S. A. H. Banuazizi, S. R. Sani, A. Eklund, M. M. Naiini, S. M. Mohseni, S. Chung, P. Durrenfeld, B. G. Malm, and J. Akerman, "*Order of magnitude improvement of nano-contact spin torque nano-oscillator performance*", Nanoscale **9**, 1896–1900 (2017).

[21] P. Dürrenfeld, E. Iacocca, J. Åkerman, and P. K. Muduli, "*Parametric excitation in a magnetic tunnel junction-based spin torque oscillator*", Appl. Phys. Lett. **104**, 052410 (2014).

[22] P. K. Muduli, O. G. Heinonen, and J. Åkerman, "*Decoherence and Mode Hopping in a Magnetic Tunnel Junction Based Spin Torque Oscillator*", Phys. Rev. Lett. **108**, 207203 (2012).

[23] P. K. Muduli, O. G. Heinonen, and J. Åkerman, "*Bias dependence of perpendicular spin torque and of free- and fixed-layer eigenmodes in MgO-based nanopillars*", Phys. Rev. B **83**, 184410 (2011).

[24] P. Dürrenfeld, E. Iacocca, J. Åkerman, and P. K. Muduli, "*Parametric excitation in a magnetic tunnel junction-based spin torque oscillator*", Appl. Phys. Lett. **104**, 052410 (2014).

[25] D. Tiwari, N. Sisodia, R. Sharma, P. Dürrenfeld, J. Åkerman, and P. K. Muduli, "*Enhancement of spin-torque diode sensitivity in a magnetic tunnel junction by parametric synchronization*", Appl. Phys. Lett. **108**, 082402 (2016).

[26] H. Mazraati, T. Q. Le, A. A. Awad, S. Chung, E. Hirayama, S. Ikeda, F. Matsukura, H. Ohno, and J. Åkerman, "*Free- and reference-layer magnetization modes versus in-plane magnetic field in a magnetic tunnel junction with perpendicular magnetic easy axis*", Phys. Rev. B **94**, 104428 (2016).

[27] M. Zahedinejad, A. A. Awad, P. Dürrenfeld, A. Houshang, Y. Yin, P. K. Muduli, and J. Åkerman, "*Current Modulation of Nanoconstriction Spin-Hall Nano-Oscillators*", IEEE Magn. Lett. **8**, 1–4 (2017).

[28] P. Durrenfeld, A. A. Awad, A. Houshang, R. K. Dumas, and J. Akerman, "*A 20 nm spin Hall nano-oscillator*", Nanoscale **9**, 1285–1291 (2017).

[29] H. Mazraati, S. Chung, A. Houshang, M. Dvornik, L. Piazza, F. Qejvanaj, S. Jiang, T. Q. Le, J. Weissenrieder, and J. Åkerman, "*Low operational current spin Hall nano-oscillators based on NiFe/W bilayers*", Appl. Phys. Lett. **109**, 242402 (2016).

[30] J. Slonczewski, "*Excitation of spin waves by an electric current*", J. Magn. Magn. Mater. **195**, 261–268 (1999).

[31] S. Bonetti, V. Tiberkevich, G. Consolo, G. Finocchio, P. Muduli, F. Mancoff, A. Slavin, and J. Åkerman, "*Experimental Evidence of Self-Localized and Propagating Spin Wave Modes in Obliquely Magnetized Current-Driven Nanocontacts*", Phys. Rev. Lett. **105**, 217204 (2010).

[32] M. Madami, S. Bonetti, G. Consolo, S. Tacchi, G. Carlotti, G. Gubbiotti, F. B. Mancoff, M. A. Yar, and J. Åkerman, "*Direct observation of a propagating spin wave induced by spin-transfer torque*", Nature Nanotech. **6**, 635–638 (2011).

[33] A. Slavin and V. Tiberkevich, "*Spin Wave Mode Excited by Spin-Polarized Current in a Magnetic Nanocontact is a Standing Self-Localized Wave Bullet*", Phys. Rev. Lett. **95**, 237201 (2005).

[34] G. Gerhart, E. Bankowski, G. A. Melkov, V. S. Tiberkevich, and A. N. Slavin, "*Angular dependence of the microwave-generation threshold in a nanoscale spin-torque oscillator*", Phys. Rev. B **76**, 024437 (2007).

[35] V. E. Demidov, S. Urazhdin, and S. O. Demokritov, "*Direct observation and mapping of spin waves emitted by spin-torque nano-oscillators*", Nature Mater. **9**, 984–988 (2010).

[36] R. K. Dumas, E. Iacocca, S. Bonetti, S. R. Sani, S. M. Mohseni, A. Eklund, J. Persson, O. Heinonen, and J. Åkerman, "*Spin-Wave-Mode Coexistence on the Nanoscale: A Consequence of the Oersted-Field-Induced Asymmetric Energy Landscape*", Phys. Rev. Lett. **110**, 257202 (2013).

[37] M. A. Hoefer, T. J. Silva, and M. W. Keller, "*Theory for a dissipative droplet soliton excited by a spin torque nanocontact*", Phys. Rev. B **82**, 054432 (2010).

[38] S. M. Mohseni, S. R. Sani, J. Persson, T. N. A. Nguyen, S. Chung, Y. Pogoryelov, P. K. Muduli, E. Iacocca, A. Eklund, R. K. Dumas, S. Bonetti, A. Deac, M. A. Hoefer, and J. Åkerman, "*Spin Torque–Generated Magnetic Droplet Solitons*", Science **339**, 1295–1298 (2013).

[39] F. Macià, D. Backes, and A. D. Kent, "*Stable magnetic droplet solitons in spin-transfer nanocontacts*", Nature Nanotech. **9**, 992–996 (2014).

[40] D. Xiao, V. Tiberkevich, Y. H. Liu, Y. W. Liu, S. M. Mohseni, S. Chung, M. Ahlberg, A. N. Slavin, J. Åkerman, and Y. Zhou, "*Parametric autoexcitation of magnetic droplet soliton perimeter modes*", Phys. Rev. B **95**, 024106 (2017).

[41] C. Wang, D. Xiao, Y. Zhou, J. Åkerman, and Y. Liu, "*Phase-locking of multiple magnetic droplets by a microwave magnetic field*", AIP Advances **7**, 056019 (2017).

[42] S. Chung, S. M. Mohseni, A. Eklund, P. Dürrenfeld, M. Ranjbar, S. R. Sani, T. N. A. Nguyen, R. K. Dumas, and J. Åkerman, "*Magnetic droplet solitons in orthogonal spin valves*", Low Temp. Phys. **41**, 833–837 (2015).

[43] E. Iacocca, R. K. Dumas, L. Bookman, M. Mohseni, S. Chung, M. A. Hoefer, and J. Åkerman, "*Confined Dissipative Droplet Solitons in Spin-Valve Nanowires with Perpendicular Magnetic Anisotropy*", Phys. Rev. Lett. **112**, 047201 (2014).

[44] S. M. Mohseni, S. R. Sani, R. K. Dumas, J. Persson, T. N. Anh Nguyen, S. Chung, Y. Pogoryelov, P. K. Muduli, E. Iacocca, A. Eklund, and J. Åkerman, "*Magnetic droplet solitons in orthogonal nano-contact spin torque oscillators*", Physica B **435**, 84–87 (2014).

[45] D. Xiao, Y. Liu, Y. Zhou, S. M. Mohseni, S. Chung, and J. Åkerman, "*Merging droplets in double nanocontact spin torque oscillators*", Phys. Rev. B **93**, 094431 (2016).

[46] S. Chung, A. Eklund, E. Iacocca, S. M. Mohseni, S. R. Sani, L. Bookman, M. A. Hoefer, R. K. Dumas, and J. Åkerman, "*Magnetic droplet nucleation boundary in orthogonal spin-torque nano-oscillators*", Nat. Commun. **7**, 11209– (2016).

[47] S. Bonetti, P. Muduli, F. Mancoff, and J. Åkerman, "*Spin torque oscillator frequency versus magnetic field angle: The prospect of operation beyond 65 GHz*", Appl. Phys. Lett. **94**, 102507 (2009).

[48] S. M. Mohseni, S. R. Sani, J. Persson, T. N. Anh Nguyen, S. Chung, Y. Pogoryelov, and J. Åkerman, "*High frequency operation of a spin-torque oscillator at low field*", Phys. Status Solidi RRL **5**, 432–434 (2011).

[49] P. K. Muduli, O. G. Heinonen, and J. Åkerman, "*Intrinsic frequency doubling in a magnetic tunnel junction-based spin torque oscillator*", J. Appl. Phys. **110**, 076102 (2011).

[50] P. K. Muduli, Y. Pogoryelov, G. Consolo, F. Mancoff, and J. Åkerman, "*Modulation of single and double spin torque oscillators*", AIP Conference Proceedings **1347**, 318–321 (2011).

[51] P. K. Muduli, Y. Pogoryelov, F. Mancoff, and J. Åkerman, "*Modulation of Individual and Mutually Synchronized Nanocontact-Based Spin Torque Oscillators*", IEEE Trans. Magn. **47**, 1575–1579 (2011).

[52] P. K. Muduli, Y. Pogoryelov, Y. Zhou, F. Mancoff, and J. Åkerman, "*Spin Torque Oscillators and RF Currents–Modulation, Locking, and Ringing*", Integr. Ferroelectr. **125**, 147–154 (2011).

[53] Y. Pogoryelov, P. K. Muduli, S. Bonetti, F. Mancoff, and J. Åkerman, "*Spin-torque oscillator linewidth narrowing under current modulation*", Appl. Phys. Lett. **98**, 192506 (2011).

[54] Y. Pogoryelov, P. K. Muduli, S. Bonetti, E. Iacocca, F. Mancoff, and J. Åkerman, "*Frequency modulation of spin torque oscillator pairs*", Appl. Phys. Lett. **98**, 192501 (2011).

[55] Y. Pogoryelov, P. K. Muduli, and J. Åkerman, "*Combined Wide-Narrow Double Modulation of Spin-Torque Oscillators for Improved Linewidth During Communication*", IEEE Trans. Magn. **48**, 4077–4080 (2012).

[56] E. Iacocca and J. Åkerman, "*Analytical investigation of modulated spin-torque oscillators in the framework of coupled differential equations with variable coefficients*", Phys. Rev. B **85**, 184420 (2012).

[57] V. Puliafito, Y. Pogoryelov, B. Azzerboni, J. Åkerman, and G. Finocchio, "*Hysteretic Synchronization in Spin-Torque Nanocontact Oscillators: A Micromagnetic Study*", IEEE Trans. Nanotechnol. **13**, 532–536 (2014).

[58] Y. Zhou, V. Tiberkevich, G. Consolo, E. Iacocca, B. Azzerboni, A. Slavin, and J. Åkerman, "*Oscillatory transient regime in the forced dynamics of a nonlinear auto oscillator*", Phys. Rev. B **82**, 012408 (2010).

[59] Y. Zhou and J. Åkerman, "*Perpendicular spin torque promotes synchronization of magnetic tunnel junction based spin torque oscillators*", Appl. Phys. Lett. **94**, 112503 (2009).

[60] Y. Zhou, S. Bonetti, J. Persson, and J. Åkerman, "*Capacitance Enhanced Synchronization of Pairs of Spin-Transfer Oscillators*", IEEE Trans. Magn. **45**, 2421–2423 (2009).

[61] D. Li, Y. Zhou, B. Hu, J. Åkerman, and C. Zhou, "*Multiple synchronization attractors of serially connected spin-torque nanooscillators*", Phys. Rev. B **86**, 014418 (2012).

[62] F. B. Mancoff, N. D. Rizzo, B. N. Engel, and S. Tehrani, "*Phase-locking in double-point-contact spin-transfer devices*", Nature **437**, 393–395 (2005).

[63] S. Kaka, M. R. Pufall, W. H. Rippard, T. J. Silva, S. E. Russek, and J. A. Katine, "*Mutual phase-locking of microwave spin torque nano-oscillators*", Nature **437**, 389–392 (2005).

[64] S. Sani, J. Persson, S. Mohseni, Y. Pogoryelov, P. Muduli, A. Eklund, G. Malm, M. Käll, A. Dmitriev, and J. Åkerman, "*Mutually synchronized bottom-up multi-nanocontact spin-torque oscillators*", Nat. Commun. **4**, 2731 (2013).

[65] A. A. Awad, P. Dürrenfeld, A. Houshang, M. Dvornik, E. Iacocca, R. K. Dumas, and J. Åkerman, "*Long-range mutual synchronization of spin Hall nano-oscillators*", Nature Phys. **13**, 292–299 (2017).

[66] G. Gubbiotti, S. Tacchi, M. Madami, G. Carlotti, Z. Yang, J. Ding, A. O. Adeyeye, and M. Kostylev, "*Collective spin excitations in bicomponent magnonic crystals consisting of bilayer permalloy/Fe nanowires*", Phys. Rev. B **93**, 184411 (2016).

[67] P. S. Keatley, S. R. Sani, G. Hrkac, S. M. Mohseni, P. Dürrenfeld, T. H. J. Loughran, J. Åkerman, and R. J. Hicken, "*Direct observation of magnetization dynamics generated by nanocontact spin-torque vortex oscillators*", Phys. Rev. B **94**, 060402 (2016).

[68] P. S. Keatley, S. R. Sani, G. Hrkac, S. M. Mohseni, P. Dürrenfeld, J. Åkerman, and R. J. Hicken, "*Imaging magnetisation dynamics in nano-contact spin-torque vortex oscillators exhibiting gyrotropic mode splitting*", J. Phys. D: Appl. Phys. **50**, 164003 (2017).

[69] R. Sharma, P. Dürrenfeld, E. Iacocca, O. G. Heinonen, J. Åkerman, and P. K. Muduli, "*Mode-hopping mechanism generating colored noise in a magnetic tunnel junction based spin torque oscillator*", Appl. Phys. Lett. **105**, 132404 (2014).

[70] E. Iacocca, O. Heinonen, P. K. Muduli, and J. Åkerman, "*Generation linewidth of mode-hopping spin torque oscillators*", Phys. Rev. B **89**, 054402 (2014).

[71] A. Eklund, S. Bonetti, S. R. Sani, S. M. Mohseni, J. Persson, S. Chung, S. A. H. Banuazizi, E. Iacocca, M. Östling, J. Åkerman, and B. G. Malm, "*Dependence of the colored frequency noise in spin torque oscillators on current and magnetic field*", Appl. Phys. Lett. **104**, 092405 (2014).

[72] P. K. Muduli, O. G. Heinonen, and J. Åkerman, "*Temperature dependence of linewidth in nanocontact based spin torque oscillators: Effect of multiple oscillatory modes*", Phys. Rev. B **86**, 174408 (2012).

[73] E. Iacocca, P. Dürrenfeld, O. Heinonen, J. Åkerman, and R. K. Dumas, "*Mode-coupling mechanisms in nanocontact spin-torque oscillators*", Phys. Rev. B **91**, 104405 (2015).

[74] E. Iacocca and J. Åkerman, "*Destabilization of serially connected spin-torque oscillators via non-Adlerian dynamics*", J. Appl. Phys. **110**, 103910 (2011).

[75] S. Yuasa, T. Nagahama, A. Fukushima, Y. Suzuki, and K. Ando, "*Giant room-temperature magnetoresistance in single-crystal Fe/MgO/Fe magnetic tunnel junctions*", Nature Mater. **3**, 868–871 (2004).

[76] S. Bonetti, "Magnetization Dynamics in Nano-Contact Spin Torque Oscillators - Solitonic bullets and propagating spin waves", PhD thesis (KTH - Royal Institute of Technology, 2010).

[77] T. Shinjo, *Nanomagnetism and spintronics* (Elsevier, 2013).

[78] A. M. Deac, A. Fukushima, H. Kubota, H. Maehara, Y. Suzuki, S. Yuasa, Y. Nagamine, K. Tsunekawa, D. D. Djayaprawira, and N. Watanabe, "*Bias-driven high-power microwave emission from MgO-based tunnel magnetoresistance devices*", Nature Phys. **4**, 803–809 (2008).

[79] D. D. Djayaprawira, K. Tsunekawa, M. Nagai, H. Maehara, S. Yamagata, N. Watanabe, S. Yuasa, Y. Suzuki, and K. Ando, "*230% room-temperature magnetoresistance in CoFeB/MgO/CoFeB magnetic tunnel junctions*", Appl. Phys. Lett. **86**, 092502 (2005).

[80] W. Thomson, "*On the Electro-Dynamic Qualities of Metals:–Effects of Magnetization on the Electric Conductivity of Nickel and of Iron*", Proc. R. Soc. London **8**, 546–550 (1856).

[81] T. McGuire and R. Potter, "*Anisotropic magnetoresistance in ferromagnetic 3d alloys*", IEEE Trans. Magn. **11**, 1018–1038 (1975).

[82] F. J. Yang, Y. Sakuraba, S. Kokado, Y. Kota, A. Sakuma, and K. Takanashi, "*Anisotropic magnetoresistance in Co_2(Fe,Mn)Si Heusler epitaxial films: A fingerprint of half-metallicity*", Phys. Rev. B **86**, 020409 (2012).

[83] M. N. Baibich, J. M. Broto, A. Fert, F. N. Van Dau, F. Petroff, P. Etienne, G. Creuzet, A. Friederich, and J. Chazelas, "*Giant Magnetoresistance of (001)Fe/(001)Cr Magnetic Superlattices*", Phys. Rev. Lett. **61**, 2472–2475 (1988).

[84] G. Binasch, P. Grünberg, F. Saurenbach, and W. Zinn, "*Enhanced magnetoresistance in layered magnetic structures with antiferromagnetic interlayer exchange*", Phys. Rev. B **39**, 4828–4830 (1989).

[85] N. F. Mott, "*The Electrical Conductivity of Transition Metals*", Proc. R. Soc. A **153**, 699–717 (1936).

[86] J.-G. (Zhu and C. Park, "*Magnetic tunnel junctions*", Mater. Today **9**, 36–45 (2006).

[87] E. H. Hall, "*On a New Action of the Magnet on Electric Currents*", Amer. J. Math. **2**, 287–292 (1879).

[88] E. H. Hall, "*On the "Rotational Coefficient" in Nickel and Cobalt*", Proc. Phys. Soc. London **4**, 325 (1880).

[89] E. M. Pugh and N. Rostoker, "*Hall Effect in Ferromagnetic Materials*", Rev. Mod. Phys. **25**, 151–157 (1953).

[90] J. E. Hirsch, "*Spin Hall Effect*", Phys. Rev. Lett. **83**, 1834–1837 (1999).

[91] A. Hoffmann, "*Spin Hall Effects in Metals*", IEEE Trans. Magn. **49**, 5172–5193 (2013).

[92] L. Liu, T. Moriyama, D. C. Ralph, and R. A. Buhrman, "*Spin-Torque Ferromagnetic Resonance Induced by the Spin Hall Effect*", Phys. Rev. Lett. **106**, 036601 (2011).

[93] V. E. Demidov, S. Urazhdin, E. R. J. Edwards, M. D. Stiles, R. D. McMichael, and S. O. Demokritov, "*Control of Magnetic Fluctuations by Spin Current*", Phys. Rev. Lett. **107**, 107204 (2011).

[94] L. Liu, O. J. Lee, T. J. Gudmundsen, D. C. Ralph, and R. A. Buhrman, "*Current-Induced Switching of Perpendicularly Magnetized Magnetic Layers Using Spin Torque from the Spin Hall Effect*", Phys. Rev. Lett. **109**, 096602 (2012).

[95] R. Karplus and J. M. Luttinger, "*Hall Effect in Ferromagnetics*", Phys. Rev. **95**, 1154–1160 (1954).

[96] L. Berger, "*Side-Jump Mechanism for the Hall Effect of Ferromagnets*", Phys. Rev. B **2**, 4559–4566 (1970).

[97] J. Smit, "*The spontaneous hall effect in ferromagnetics II*", Physica **24**, 39–51 (1958).

[98] G. Y. Guo, S. Murakami, T.-W. Chen, and N. Nagaosa, "*Intrinsic Spin Hall Effect in Platinum: First-Principles Calculations*", Phys. Rev. Lett. **100**, 096401 (2008).

[99] T. Tanaka, H. Kontani, M. Naito, T. Naito, D. S. Hirashima, K. Yamada, and J. Inoue, "*Intrinsic spin Hall effect and orbital Hall effect in* 4*d and* 5*d transition metals*", Phys. Rev. B **77**, 165117 (2008).

[100] H. Kontani, T. Tanaka, D. S. Hirashima, K. Yamada, and J. Inoue, "*Giant Orbital Hall Effect in Transition Metals: Origin of Large Spin and Anomalous Hall Effects*", Phys. Rev. Lett. **102**, 016601 (2009).

[101] A. Slavin and V. Tiberkevich, "*Nonlinear Auto-Oscillator Theory of Microwave Generation by Spin-Polarized Current*", IEEE Trans. Magn. **45**, 1875–1918 (2009).

[102] T. Silva and M. Keller, "*Theory of Thermally Induced Phase Noise in Spin Torque Oscillators for a High-Symmetry Case*", IEEE Trans. Magn. **46**, 3555–3573 (2010).

[103] M. W. Keller, M. R. Pufall, W. H. Rippard, and T. J. Silva, "*Nonwhite frequency noise in spin torque oscillators and its effect on spectral linewidth*", Phys. Rev. B **82**, 054416 (2010).

[104] S. Bonetti, V. Puliafito, G. Consolo, V. S. Tiberkevich, A. N. Slavin, and J. Åkerman, "*Power and linewidth of propagating and localized modes in nanocontact spin-torque oscillators*", Phys. Rev. B **85**, 174427 (2012).

[105] P. K. Muduli, Y. Pogoryelov, S. Bonetti, G. Consolo, F. Mancoff, and J. Åkerman, "*Nonlinear frequency and amplitude modulation of a nanocontact-based spin-torque oscillator*", Phys. Rev. B **81**, 140408 (2010).

[106] H. Maehara, H. Kubota, Y. Suzuki, T. Seki, K. Nishimura, N. Yoshinori, K. Tsunekawa, A. Fukushima, A. M. Deac, K. Ando, and S. Yuasa, "*Large Emission Power over 2 μW with High Q Factor Obtained from Nanocontact Magnetic-Tunnel-Junction-Based Spin Torque Oscillator*", Appl. Phys. Express **6**, 113005 (2013).

[107] H. Maehara, H. Kubota, Y. Suzuki, T. Seki, K. Nishimura, Y. Nagamine, K. Tsunekawa, A. Fukushima, A. M. Deac, K. Ando, and S. Yuasa, "*Large Emission Power over 2 μW with High Q Factor Obtained from Nanocontact Magnetic-Tunnel-Junction-Based Spin Torque Oscillator*", Appl. Phys. Express **6**, 113005 (2013).

[108] C. Kittel, "*On the Theory of Ferromagnetic Resonance Absorption*", Phys. Rev. **73**, 155–161 (1948).

[109] C. Herring and C. Kittel, "*On the Theory of Spin Waves in Ferromagnetic Media*", Phys. Rev. **81**, 869–880 (1951).

[110] J. Coey, *Magnetism and Magnetic Materials* (Cambridge University Press, 2009).

[111] A. Pikovsky, M. Rosenblum, and J. Kurths, *Synchronization : a universal concept in nonlinear sciences*, The Cambridge nonlinear science series (Cambridge University Press, Cambridge, 2001).

[112] M. R. Pufall, W. H. Rippard, S. E. Russek, S. Kaka, and J. A. Katine, "*Electrical Measurement of Spin-Wave Interactions of Proximate Spin Transfer Nanooscillators*", Phys. Rev. Lett. **97**, 087206 (2006).

[113] S. R. Sani, "Fabrication and Characterization of Nanocontact Spin-Torque Oscillators", PhD thesis (KTH - Royal Institute of Technology, 2013).

[114] P. Dürrenfeld, "Spin Torque and Spin Hall Oscillators with Single Magnetic Layers", PhD thesis (University of Gothenburg, 2015).

[115] W. H. Rippard, M. R. Pufall, and T. J. Silva, "*Quantitative studies of spin-momentum-transfer-induced excitations in Co/Cu multilayer films using point-contact spectroscopy*", Appl. Phys. Lett. **82**, 1260 (2003).

[116] S. Mangin, D. Ravelosona, J. A. Katine, M. J. Carey, B. D. Terris, and E. E. Fullerton, "*Current-induced magnetization reversal in nanopillars with perpendicular anisotropy*", Nature Mater. **5**, 210–215 (2006).

[117] C. H. Sim, M. Moneck, T. Liew, and J.-G. Zhu, "*Frequency-tunable perpendicular spin torque oscillator*", J. Appl. Phys. **111**, 07C914 (2012).

[118] W. H. Rippard, A. M. Deac, M. R. Pufall, J. M. Shaw, M. W. Keller, S. E. Russek, G. E. W. Bauer, and C. Serpico, "*Spin-transfer dynamics in spin valves with out-of-plane magnetized CoNi free layers*", Phys. Rev. B **81**, 014426 (2010).

[119] D. Houssameddine, U. Ebels, B. Delaet, B. Rodmacq, I. Firastrau, F. Ponthenier, M. Brunet, C. Thirion, J.-P. Michel, L. Prejbeanu-Buda, M.-C. Cyrille, O. Redon, and B. Dieny, "*Spin-torque oscillator using a perpendicular polarizer and a planar free layer*", Nature Mater. **6**, 447–453 (2007).

[120] S. M. Mohseni, S. R. Sani, J. Persson, T. N. Anh Nguyen, S. Chung, Y. Pogoryelov, and J. Åkerman, "*High frequency operation of a spin-torque oscillator at low field*", Phys. Status Solidi Rapid Res. Lett. **5**, 432–434 (2011).

[121] S. Chung, S. M. Mohseni, S. R. Sani, E. Iacocca, R. K. Dumas, T. N. Anh Nguyen, Y. Pogoryelov, P. K. Muduli, A. Eklund, M. Hoefer, and J. Åkerman, "*Spin transfer torque generated magnetic droplet solitons (invited)*", J. Appl. Phys. **115**, 172612 (2014).

[122] Y. Zhou, C. L. Zha, S. Bonetti, J. Persson, and J. Åkerman, "*Spin-torque oscillator with tilted fixed layer magnetization*", Appl. Phys. Lett. **92**, 262508 (2008).

[123] Y. Zhou, C. L. Zha, S. Bonetti, J. Persson, and J. Åkerman, "*Microwave generation of tilted-polarizer spin torque oscillator*", J. Appl. Phys. **105**, 07D116 (2009).

[124] Y. Zhou, S. Bonetti, C. L. Zha, and J. Åkerman, "*Zero-field precession and hysteretic threshold currents in a spin torque nano device with tilted polarizer*", New J. Phys. **11**, 103028 (2009).

[125] P.-B. He, R.-X. Wang, Z.-D. Li, Q.-H. Liu, A.-L. Pan, Y.-G. Wang, and B.-S. Zou, "*Current-driven magnetization dynamics in magnetic trilayers with a tilted spin polarizer*", Eur. Phys. J. B **73**, 417–421 (2010).

[126] T. A. Nguyen, N. Benatmane, V. Fallahi, Y. Fang, S. Mohseni, R. Dumas, and J. Åkerman, "*[Co/Pd]$_4$-Co-Pd-NiFe spring magnets with highly tunable and uniform magnetization tilt angles*", J. Magn. Magn. Mater. **324**, 3929–3932 (2012).

[127] S. Chung, S. M. Mohseni, V. Fallahi, T. N. Anh Nguyen, N. Benatmane, R. K. Dumas, and J. Åkerman, "*Tunable spin configuration in [Co/Ni]-NiFe spring magnets*", J. Phys. D: Appl. Phys. **46**, 125004 (2013).

[128] S. Tacchi, T. N. A. Nguyen, G. Gubbiotti, M. Madami, G. Carlotti, M. G. Pini, A. Rettori, V. Fallahi, R. K. Dumas, and J. Åkerman, "*[Co/Pd]-CoFeB exchange spring magnets with tunable gap of spin wave excitations*", J. Phys. D: Appl. Phys. **47**, 495004 (2014).

[129] S. Tacchi, T. N. A. Nguyen, G. Carlotti, G. Gubbiotti, M. Madami, R. K. Dumas, J. W. Lau, J. Åkerman, A. Rettori, and M. G. Pini, "*Spin wave excitations in exchange-coupled [Co/Pd]-NiFe films with tunable tilting of the magnetization*", Phys. Rev. B **87**, 144426 (2013).

[130] T. N. A. Nguyen, R. Knut, V. Fallahi, S. Chung, Q. T. Le, S. M. Mohseni, O. Karis, S. Peredkov, R. K. Dumas, C. W. Miller, and J. Åkerman, "*Depth-Dependent Magnetization Profiles of Hybrid Exchange Springs*", Phys. Rev. Applied **2**, 044014 (2014).

[131] T. N. A. Nguyen, Y. Fang, V. Fallahi, N. Benatmane, S. M. Mohseni, R. K. Dumas, and J. Åkerman, "*[Co/Pd]–NiFe exchange springs with tunable magnetization tilt angle*", Appl. Phys. Lett. **98**, 172502 (2011).

[132] G. Consolo, B. Azzerboni, G. Gerhart, G. A. Melkov, V. Tiberkevich, and A. N. Slavin, "*Excitation of self-localized spin-wave bullets by spin-polarized current in in-plane magnetized magnetic nanocontacts: A micromagnetic study*", Phys. Rev. B **76**, 144410 (2007).

[133] G. Consolo, L. Lopez-Diaz, L. Torres, and B. Azzerboni, "*Magnetization dynamics in nanocontact current controlled oscillators*", Phys. Rev. B **75**, 214428 (2007).

[134] G. Consolo, B. Azzerboni, L. Lopez-Diaz, G. Gerhart, E. Bankowski, V. Tiberkevich, and A. Slavin, "*Micromagnetic study of the above-threshold generation regime in a spin-torque oscillator based on a magnetic nanocontact magnetized at an arbitrary angle*", Phys. Rev. B **78**, 014420 (2008).

[135] G. Consolo, G. Finocchio, G. Siracusano, S. Bonetti, A. Eklund, J. Åkerman, and B. Azzerboni, "*Non-stationary excitation of two localized spin-wave modes in a nano-contact spin torque oscillator*", J. Appl. Phys. **114**, 153906 (2013).

[136] O. Heinonen, P. Muduli, E. Iacocca, and J. Akerman, "*Decoherence, Mode Hopping, and Mode Coupling in Spin Torque Oscillators*", IEEE Trans. Magn. **49**, 4398–4404 (2013).

[137] M. Madami, E. Iacocca, S. Sani, G. Gubbiotti, S. Tacchi, R. K. Dumas, J. Åkerman, and G. Carlotti, "*Propagating spin waves excited by spin-transfer torque: A combined electrical and optical study*", Phys. Rev. B **92**, 024403 (2015).

[138] M. A. Hoefer, T. J. Silva, and M. D. Stiles, "*Model for a collimated spin-wave beam generated by a single-layer spin torque nanocontact*", Phys. Rev. B **77**, 144401 (2008).

[139] A. Vansteenkiste, J. Leliaert, M. Dvornik, M. Helsen, F. Garcia-Sanchez, and B. Van Waeyenberge, "*The design and verification of MuMax3*", AIP Adv. **4**, 107133 (2014).

[140] I. Lee, Y. Obukhov, G. Xiang, A. Hauser, F. Yang, P. Banerjee, D. V. Pelekhov, and P. C. Hammel, "*Nanoscale scanning probe ferromagnetic resonance imaging using localized modes*", Nature **466**, 845–848 (2010).

[141] S. Petit-Watelot, R. M. Otxoa, M. Manfrini, W. Van Roy, L. Lagae, J.-V. Kim, and T. Devolder, "*Understanding Nanoscale Temperature Gradients in Magnetic Nanocontacts*", Phys. Rev. Lett. **109**, 267205 (2012).

[142] S. S. Kalarickal, P. Krivosik, M. Wu, C. E. Patton, M. L. Schneider, P. Kabos, T. J. Silva, and J. P. Nibarger, "*Ferromagnetic resonance linewidth in metallic thin films: Comparison of measurement methods*", J. Appl. Phys. **99**, 093909 (2006).

[143] T. Kizuka and H. Aoki, "*The Dynamics of Electromigration in Copper Nanocontacts*", Appl. Phys. Express **2**, 075003 (2009).

[144] Y. K. Kato, R. C. Myers, A. C. Gossard, and D. D. Awschalom, "*Observation of the Spin Hall Effect in Semiconductors*", Science **306**, 1910–1913 (2004).

[145] J. Sinova, S. O. Valenzuela, J. Wunderlich, C. H. Back, and T. Jungwirth, "*Spin Hall effects*", Rev. Mod. Phys. **87**, 1213–1260 (2015).

[146] M. Evelt, V. E. Demidov, V. Bessonov, S. O. Demokritov, J. L. Prieto, M. Muñoz, J. B. Youssef, V. V. Naletov, G. de Loubens, O. Klein, M. Collet, K. Garcia-Hernandez, P. Bortolotti, V. Cros, and A. Anane, "*High-efficiency control of spin-wave propagation in ultra-thin yttrium iron garnet by the spin-orbit torque*", Appl. Phys. Lett. **108**, 172406 (2016).

[147] R. K. Dumas and J. Akerman, "*Spintronics: Channelling spin waves*", Nature Nanotech. **9**, 503–504 (2014).

[148] L. Liu, C.-F. Pai, Y. Li, H. W. Tseng, D. C. Ralph, and R. A. Buhrman, "*Spin-Torque Switching with the Giant Spin Hall Effect of Tantalum*", Science **336**, 555–558 (2012).

[149] L. Yang, R. Verba, V. Tiberkevich, T. Schneider, A. Smith, Z. Duan, B. Youngblood, K. Lenz, J. Lindner, A. N. Slavin, and I. N. Krivorotov, "*Reduction of phase noise in nanowire spin orbit torque oscillators*", Sci. Rep. **5**, 16942 (2015).

[150] M. Ranjbar, P. Dürrenfeld, M. Haidar, E. Iacocca, M. Balinskiy, T. Le, M. Fazlali, A. Houshang, A. Awad, R. Dumas, and J. Åkerman, "*CoFeB-Based Spin Hall Nano-Oscillators*", IEEE Magn. Lett. **5**, 3000504 (2014).

[151] T. Kendziorczyk, S. O. Demokritov, and T. Kuhn, "*Spin-wave-mediated mutual synchronization of spin-torque nano-oscillators: A micromagnetic study of multistable phase locking*", Phys. Rev. B **90**, 054414 (2014).

[152] Y. Yin, F. Pan, M. Ahlberg, M. Ranjbar, P. Dürrenfeld, A. Houshang, M. Haidar, L. Bergqvist, Y. Zhai, R. K. Dumas, A. Delin, and J. Åkerman, "*Tunable permalloy-based films for magnonic devices*", Phys. Rev. B **92**, 024427 (2015).

[153] Y. Yin, M. Ahlberg, P. Dürrenfeld, Y. Zhai, R. K. Dumas, and J. Åkerman, "*Ferromagnetic and Spin-Wave Resonance on Heavy-Metal-Doped Permalloy Films: Temperature Effects*", IEEE Magn. Lett. **8**, 1–4 (2017).

[154] A. Giordano, M. Carpentieri, A. Laudani, G. Gubbiotti, B. Azzerboni, and G. Finocchio, "*Spin-Hall nano-oscillator: A micromagnetic study*", Appl. Phys. Lett. **105**, 042412 (2014).

[155] K. Kudo, T. Nagasawa, K. Mizushima, H. Suto, and R. Sato, "*Numerical Simulation on Temporal Response of Spin-Torque Oscillator to Magnetic Pulses*", Appl. Phys. Express **3**, 043002 (2010).

[156] P. M. Braganca, B. A. Gurney, B. A. Wilson, J. A. Katine, S. Maat, and J. R. Childress, "*Nanoscale magnetic field detection using a spin torque oscillator*", Nanotechnology **21**, 235202 (2010).

[157] E. R. Evarts, M. R. Pufall, and W. H. Rippard, "*Continuous-film vs. device-level ferromagnetic resonance in magnetic tunnel junction thin films*", J. Appl. Phys. **113**, 083903 (2013).

[158] C. Bilzer, T. Devolder, J.-V. Kim, G. Counil, C. Chappert, S. Cardoso, and P. P. Freitas, "*Study of the dynamic magnetic properties of soft CoFeB films*", J. Appl. Phys. **100**, 053903 (2006).

[159] T. Chen, A. Eklund, E. Iacocca, S. Rodriguez, B. G. Malm, J. Åkerman, and A. Rusu, "*Comprehensive and Macrospin-Based Magnetic Tunnel Junction Spin Torque Oscillator Model-Part I: Analytical Model of the MTJ STO*", IEEE Trans. Electr. Dev. **62**, 1037–1044 (2015).

[160] T. Chen, P. Dürrenfeld, S. Rodriguez, J. Åkerman, and A. Rusu, "*A highly tunable microwave oscillator based on MTJ STO technology*", Microw. Opt. Technol. Lett. **56**, 2092–2095 (2014).

[161] J. Persson, S. R. Sani, S. Bonetti, F. Magnusson, Y. Pogorylov, S. M. Mohseni, S. Gunnarsson, M. Norling, C. Stoij, and J. Akerman, "*Spin-Torque Oscillator in an Electromagnet Package*", IEEE Trans. Magn. **48**, 4378–4381 (2012).

[162] A. Khitun, M. Bao, and K. L. Wang, "*Magnonic logic circuits*", J. Phys. D: Appl. Phys. **43**, 264005 (2010).

[163] A. Khitun and K. L. Wang, "*Non-volatile magnonic logic circuits engineering*", J. Appl. Phys. **110**, 034306 (2011).

[164] F. Macià, A. D. Kent, and F. C. Hoppensteadt, "*Spin-wave interference patterns created by spin-torque nano-oscillators for memory and computation*", Nanotechnology **22**, 095301 (2011).

[165] S. Klingler, P. Pirro, T. Brächer, B. Leven, B. Hillebrands, and A. V. Chumak, "*Design of a spin-wave majority gate employing mode selection*", Appl. Phys. Lett. **105**, 152410 (2014).

[166] S. Bonetti and J. Åkerman, *Nano-Contact Spin-Torque Oscillators as Magnonic Building Blocks*, edited by S. O. Demokritov and A. N. Slavin (Springer Berlin Heidelberg, 2013), pp. 177–187.

[167] J. Grollier, D. Querlioz, and M. D. Stiles, "*Spintronic Nanodevices for Bioinspired Computing*", Proc. IEEE **104**, 2024–2039 (2016).